Article

Proteotoxic stress response drives T cell exhaustion and immune evasion

https://doi.org/10.1038/s41586-025-09539-1

Received: 12 June 2024

Accepted: 15 August 2025

Published online: 01 October 2025

Open access

Check for updates

Yi Wang[1], Anjun Ma[1,2], No-Joon Song[1], Ariana E. Shannon[1,2], Yaa S. Amankwah[1], Xingyu Chen[3], Weidong Wu[2], Ziyu Wang[1], Abbey A. Saadey[4], Amir Yousif[4], Gautam Ghosh[2], Jay K. Mandula[1], Maria Velegraki[1], Tong Xiao[1], Haitao Wen[1,4], Stanley Ching-Cheng Huang[4], Ruoning Wang[5], Christian M. Beusch[6,7], Abdelhameed S. Dawood[6], David E. Gordon[6], Mohamed S. Abdel-Hakeem[6], Hazem E. Ghoneim[1,4], Gang Xin[1,4], Brian C. Searle[1,2] & Zihai Li[1,8] ✉

Chronic infections and cancer cause T cell dysfunction known as exhaustion. This cell state is caused by persistent antigen exposure, suboptimal co-stimulation and a plethora of hostile factors that dampen protective immunity and limit the efficacy of immunotherapies[1–4]. The mechanisms that underlie T cell exhaustion remain poorly understood. Here we analyse the proteome of $CD8^+$ exhausted T (T_{ex}) cells across multiple states of exhaustion in the context of both chronic viral infections and cancer. We show that there is a non-stochastic pathway-specific discordance between mRNA and protein dynamics between T effector (T_{eff}) and T_{ex} cells. We identify a distinct proteotoxic stress response (PSR) in T_{ex} cells, which we term T_{ex}-PSR. Contrary to canonical stress responses that induce a reduction in protein synthesis[5,6], T_{ex}-PSR involves an increase in global translation activity and an upregulation of specialized chaperone proteins. T_{ex}-PSR is further characterized by the accumulation of protein aggregates and stress granules and an increase in autophagy-dominant protein catabolism. We establish that disruption of proteostasis alone can convert T_{eff} cells to T_{ex} cells, and we link T_{ex}-PSR mechanistically to persistent AKT signalling. Finally, disruption of T_{ex}-PSR-associated chaperones in $CD8^+$ T cells improves cancer immunotherapy in preclinical models. Moreover, a high T_{ex}-PSR in T cells from patients with cancer confers poor responses to clinical immunotherapy. Collectively, our findings indicate that T_{ex}-PSR is a hallmark and a mechanistic driver of T cell exhaustion, which raises the possibility of targeting proteostasis pathways as an approach for cancer immunotherapy.

T cell exhaustion represents a hypofunctional state characterized by reduced effector function and increased inhibitory receptor expression that arises from persistent antigen exposure and a hostile microenvironment[7]. T_{ex} cells observed in cancer fail to eliminate malignant cells, and this limitation mediates a key mechanism of resistance to immunotherapies[1–3]. The exhaustion program generates a heterogeneous T_{ex} cell population. Progenitor T_{ex} (T_{prog}) cells retain stemness and self-renewal capacity that respond to immune checkpoint blockade (ICB) therapies and differentiate into intermediate T (T_{int}) cells with cytolytic capacity[8–10]. Conversely, terminal T_{ex} (T_{tex}) cells accumulate over time and respond poorly to ICB therapies[8,11–13]. T cell exhaustion also limits the efficacy of chimeric antigen receptor (CAR) T cell therapy against solid tumours[14–17]. Consequently, a better understanding of T cell exhaustion is essential to overcome the limitations of current immunotherapies.

Although transcriptomic profiling has provided insights into T_{ex} cell biology, mRNA abundance is not always a faithful proxy of protein expression across various organisms[18–22]. Previous studies have revealed poor mRNA–protein correlation in T cells regardless of functional status[23–25] and the importance of post-transcriptional regulation in T cell differentiation and function[26]. In this context, a high-resolution proteomic map of T_{ex} cells would be valuable. In this study, we define the proteomic landscape of T_{ex} cells across various settings, including an in vitro exhaustion model, in vivo chronic lymphocytic choriomeningitis virus (LCMV) infection in mice, and colon tumour and bladder tumour mouse models. We demonstrate that there is pathway-specific discordance between transcript and protein levels.

We also elucidate the intricate layers of protein-level regulation pertaining to a PSR that is specific to T_{ex} cells. We show that PSR in T_{ex} cells shares similarities to unfolded protein responses and integrated stress

[1]Pelotonia Institute for Immuno-Oncology, The Ohio State University Comprehensive Cancer Center–The James, Columbus, OH, USA. [2]Department of Biomedical Informatics, College of Medicine, The Ohio State University, Columbus, OH, USA. [3]Johns Hopkins University, Baltimore, MD, USA. [4]Department of Microbial Infection and Immunity, College of Medicine, The Ohio State University, Columbus, OH, USA. [5]Center for Childhood Cancer, Hematology/Oncology and BMT, Abigail Wexner Research Institute at Nationwide Children's Hospital, Department of Pediatrics, The Ohio State University, Columbus, OH, USA. [6]Department of Pathology and Laboratory Medicine, Emory University, Atlanta, GA, USA. [7]Department of Surgical Sciences, Uppsala University, Uppsala, Sweden. [8]Division of Medical Oncology, Department of Medicine, College of Medicine, The Ohio State University, Columbus, OH, USA. ✉e-mail: Zihai.li@osumc.edu

responses. However, a marked difference is that PSR in T_{ex} cells is characterized by increased global protein synthesis. This T_{ex} cell-associated PSR signature, which we term T_{ex}-PSR, is further marked by the selective activation of chaperone proteins such as gp96 (also known as GRP94; encoded by *Hsp90b1*) and BiP (encoded by *Hspa5*) and the accumulation of protein aggregates that are predominantly driven by sustained activation of the AKT pathway. The introduction of misfolded proteins alone could convert T_{eff} cells to T_{ex} cells, which demonstrates the causality of dysregulated proteostasis in T cell exhaustion. Finally, we demonstrate that T_{ex}-PSR is also a hallmark of human T_{ex} cells in cancer and that it may contribute to resistance to cancer immunotherapy.

Discordance between RNA and protein levels

To determine whether gene expression levels reflect protein expression levels in T cells, we used an established in vitro exhaustion model that induces T cell exhaustion through repeated T cell receptor (TCR) stimulation[27,28]. We then performed parallel RNA sequencing and quantitative proteomics by mass spectrometry (MS) (Extended Data Fig. 1a). Compared with acutely activated T cells (T_{eff} cells), chronically stimulated cells (T_{ex} cells) exhibited impaired survival, proliferation and cytokine production, which were accompanied by increased expression levels of exhaustion markers, including PD1 and TIM3 (Extended Data Fig. 1b,c). To improve detection sensitivity, quantification and reproducibility, we applied the chromatogram library approach for all proteomic data collection (Extended Data Fig. 1d). The expression dynamics of key activation, exhaustion and stemness markers of T cells, such as CD25, PD1, CD39 and TCF1, obtained from the MS results aligned well with data obtained by spectral flow cytometry (Extended Data Fig. 1e).

We then ascertained whether transcript levels are a reliable surrogate for protein expression levels in T cells. In both T_{eff} and T_{ex} cells, mRNA and protein expression levels were weakly correlated, as indicated by Pearson's correlation coefficients of 0.31 and 0.38, respectively (Extended Data Fig. 2a). Moreover, the degree of correlation between RNA and protein levels did not seem to be stochastic but were functionally related (Extended Data Fig. 2b,c). A group of proteins that exhibited comparable mRNA and protein expression levels in >300 cancer cell lines[29], termed 'housekeeping' in this context, aligned well with RNA expression levels in T cells (Extended Data Fig. 2b). Proteins involved in the regulation of TCR signalling, cell death and cytokine responses exhibited a similarly strong correlation with RNA expression levels, with correlation coefficient values of around 0.7. By comparison, transcription factors (TFs) exhibited a moderate correlation between mRNA and protein expression levels, with some TFs showing detectable changes exclusively at the protein level, including FOXO1 and T-bet (Extended Data Fig. 2c,d). Furthermore, the levels of proteins associated with metabolic processes, post-transcriptional regulation and epigenetic regulation aligned poorly with mRNA levels (Extended Data Fig. 2c). The three major metabolic pathways—glycolysis, oxidative phosphorylation and fatty acid metabolism—showed discrepancies between RNA and protein levels, with most of the changes in mRNA levels not reflected at the protein level (Extended Data Fig. 2e). These results underscore the importance of directly defining the proteome rather than inferring it from the transcriptome.

PSR and specialized chaperone enrichment

We next generated a kinetic proteomic landscape of T cells during T cell exhaustion by leveraging the LCMV infection model. Antigen-specific $CD8^+$ T cell subpopulations were isolated after acute (Armstrong strain) or chronic LCMV (clone 13 strain) infection and analysed (Fig. 1a). The following endogenous $CD8^+$ T cell subpopulations specific for viral antigens (gp33 and gp276) were sorted for MS analysis at days 8 and 30 after infection: short-lived effector T cells (SLECs), memory precursor effector cells (MPECs) and central memory (T_{CM}) and effector memory (T_{EM}) T cells from Armstrong infection; and $SLAMF6^+CX3CR1^-$ T_{prog}, $CX3CR1^+$ T_{int} and $SLAMF6^-CX3CR1^-$ T_{tex} cells from clone 13 infection (Extended Data Fig. 3a). We applied a previously defined transcriptomic signature for T cell exhaustion[30] to analyse our proteomic data. Notably, in addition to increased expression of protein signatures associated with exhaustion and pro-apoptosis, T_{tex} cells exhibited a marked enrichment of proteins in the PSR pathway (Fig. 1b). We applied the same gene signatures to a single-cell RNA sequencing (scRNA-seq) dataset of mouse $gp33^+CD8^+$ T cells after LCMV clone 13 infection[31]. The upregulation of PSR in T_{ex} cells was readily discerned at the protein but not the transcript level (Extended Data Fig. 3b). We also generated a proteomic dataset of transgenic T cells against a D^b-restricted gp33 epitope of LCMV (called P14) at days 8, 15 and 30 after infection[32] (Extended Data Fig. 3c). PSR was similarly upregulated in P14 cells after clone 13 infection but not Armstrong infection (Extended Data Fig. 3d).

To further investigate proteome dynamics and PSR in T cell exhaustion, we performed proteomic analyses of T_{eff} and T_{ex} cells generated in vitro, which enabled us to achieve increased proteome coverage. T cells were collected on days 2, 4, 6 and 8 after initial activation to track proteomic dynamics during T cell activation and exhaustion as described above (Extended Data Fig. 1a). T cells exhibited distinct protein expression dynamics depending on the differentiation state (Fig. 1c). The expression dynamics of key activation, exhaustion and stemness markers, such as TCF1, SLAMF6, PD1 and TIM3, obtained by MS analyses aligned well with T cell states (Extended Data Fig. 4a). Overall, eight distinct clusters of proteins were identified (Fig. 1c and Extended Data Fig. 4b). Notably, proteins in cluster 6 were specifically upregulated in T_{ex} cells, which typically expressed exhaustion markers such as TIM3, CD39 and LAG3 (Fig. 1c), as well as molecules involved in protein transport, modification and quality control (Fig. 1d). In particular, proteins involved in the endoplasmic reticulum (ER) stress response were significantly increased as T cells became more exhausted (Fig. 1e). An increase in the expression of proteins integral to translation, transport and quality control in T_{ex} cells compared with T_{eff} cells indicates that there is an induction of a distinct PSR during the T cell exhaustion process (Fig. 1e).

We next performed a proteomic study of T cells isolated ex vivo from the tumour milieu of mouse models of MC38 colon cancer and MB49 bladder cancer (Fig. 1f). Antigen-experienced $CD44^{hi}CD8^+$ T cells were sorted by flow cytometry into T_{prog}, T_{int} and T_{tex} cells[8,11] (Fig. 1g). In the MC38 tumour model, the T_{tex} population exhibited upregulated proteins associated with the ER stress response and proteins associated with autophagy and transport (Fig. 1h). The upregulation of ER stress proteins was also observed in T cells isolated from MB49 bladder tumours (Fig. 1h).

Chaperone proteins are crucial for ensuring protein quality control. Notably, we observed a heterogeneous expression of chaperones (Fig. 1i). On the basis of their expression patterns, we categorized them into three groups: quiescence, activation and PSR chaperones (Fig. 1i). The quiescence-related chaperones showed the highest expression in naive T cells. The second group of chaperones, compromising cytosolic HSP90α and HSP90β, TRiC complex subunits (TCP1α–TCP1θ) and mitochondrial chaperone HSP75 (also known as TRAP1), were induced by TCR stimulation but reduced in T_{ex} cells, which implicated a link with T cell activation. Conversely, proteins in the third group, including several ER chaperones such as BiP and gp96, were overexpressed in T_{ex} cells, which indicated that they may have specialized roles in T cell exhaustion. These exhaustion-associated chaperones were significantly upregulated in the T_{tex} cell population from both MC38 and MB49 tumours (Fig. 1j). We performed additional analyses of proteomes of LCMV-specific T cells and tracked the expression kinetics of these chaperones during chronic infection (Extended Data Fig. 3c). Consistently, BiP, gp96 and HSPA13 were upregulated in P14 cells from mice infected with clone 13, whereas the expression of TRiC complex subunits was downregulated (Extended Data Fig. 3e). Together, these

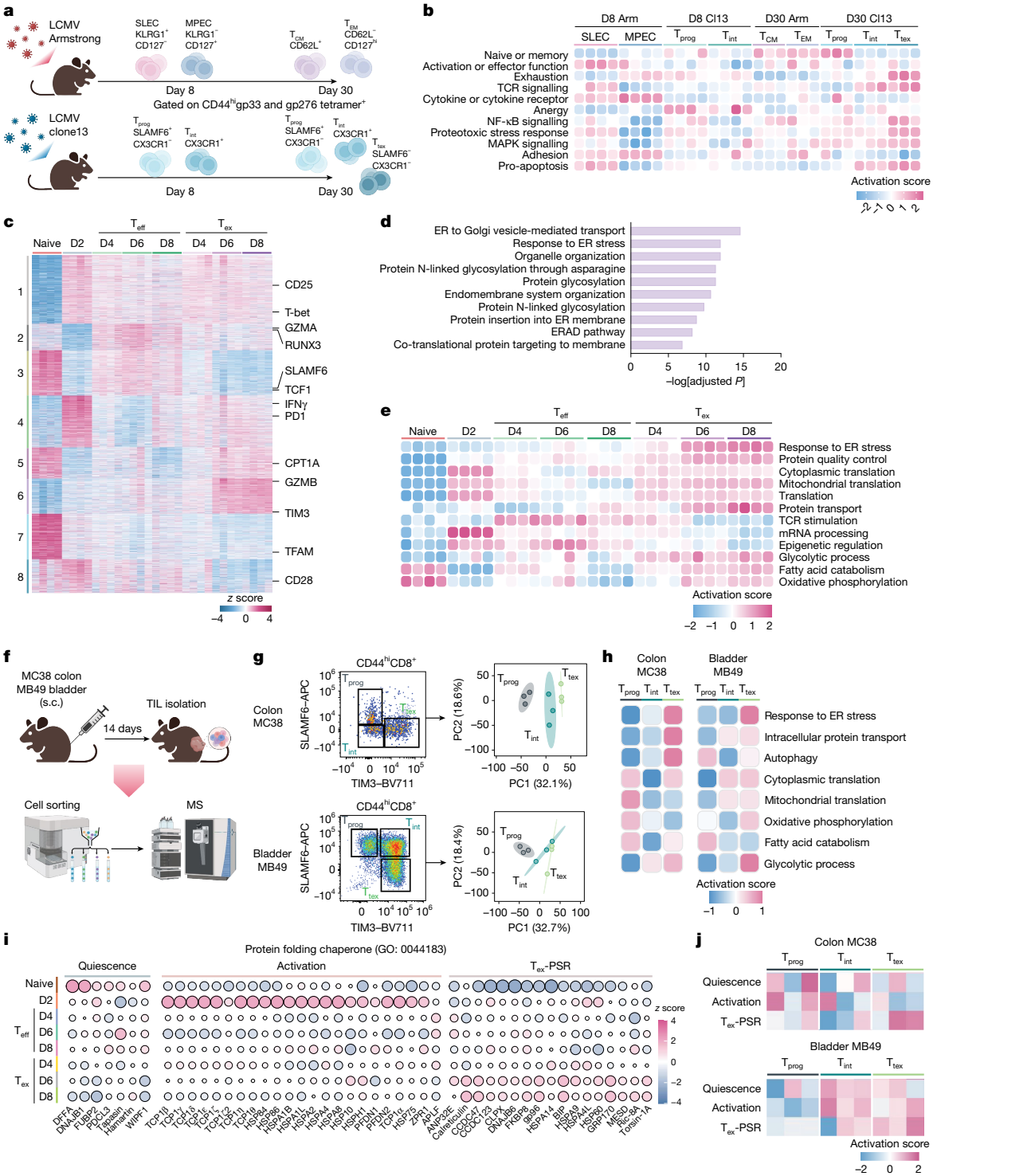

Fig. 1 | PSR is triggered in T_{ex} cells with a dynamic expression of chaperone proteins. a, Schematic of the experiment to isolate mouse splenic LCMV antigen-specific $CD8^+$ T cell subpopulations in LCMV acute (Armstrong (Arm)) and chronic (clone 13 (Cl13)) infection models. **b**, Heatmap of expression levels of proteins belonging to 11 T cell signatures across 9 groups ($n = 3–4$, representing pooled 5–15 mice per replicate). D, day. **c**, Heatmap of the expression profiles of 5,284 proteins quantified in naive T cells, acutely activated T cells (T_{eff}) and chronically activated T cells (T_{ex}) at 2, 4, 6 and 8 days after initial activation, as described in Extended Data Fig. 1a, with *k*-means clustering identifying 8 distinct expression patterns ($n = 4$, each replicate was pooled from 3 mice). **d**, Enrichment analysis of proteins from cluster 6 defined in **c** (one-sided Fisher's exact test with Benjamini–Hochberg correction). **e**, Heatmap of expression levels of proteins belonging to 12 gene ontology terms. **f**, Schematic of MS-based proteomic analysis of $CD8^+$ T cells in different exhaustion states from the MC38 colon cancer mouse model and the MB49 bladder tumour mouse model. s.c., subcutaneous. **g**, Principal component analysis plots of proteomes of T_{prog}, T_{int} and T_{tex} cells ($n = 3$, each biological replicate was pooled from 12–13 mice). **h**, Heatmap of protein expression across eight gene ontologies in three $CD8^+$ T cell subpopulations from MC38 and MB49 tumour models. **i**, Bubble plot of the expression levels of protein-folding chaperones in naive, T_{eff} and T_{ex} $CD8^+$ T cells generated in vitro as described in Extended Data Fig. 1a. The bubble colour intensity is proportional to the protein expression level. The bubble size is proportional to the absolute *z* score value. **j**, Heatmap of the expression levels of chaperone proteins (defined in **i**) in three $CD8^+$ T cell subpopulations from MC38 and MB49 tumours. The diagrams in **a** and **f** were created using BioRender (https://www.biorender.com).

findings indicate that the activation of PSR and the associated upregulation of PSR chaperones are a common hallmark of T cell exhaustion.

Dysregulated proteostasis in T_{ex} cells

Our proteomic data indicated that PSR is activated in T_{ex} cells. We next examined whether proteostasis in T_{ex} cells is disrupted. We stained T_{eff} and T_{ex} cells with the fluorescent dye NIAD-4 or its derivative CRANAD-2, which bind to amyloid-like structures enriched in misfolded proteins and aggregates[33]. T_{ex} cells showed a significant accumulation of protein aggregates compared with T_{eff} cells (Fig. 2a,b). In tumour-infiltrating T cells (TILs) isolated from MC38 and MB49 tumours, protein aggregates progressively increased as T cells became more exhausted (Fig. 2c,d). This result suggests that the protein quality control system is significantly impaired in T_{ex} cells.

The activation of PSR, the upregulation of specialized chaperone proteins and the accumulation of protein aggregates in T_{ex} cells led us to initially predict that T cell exhaustion is associated with attenuated translation to prevent further protein overload. However, this prediction was incorrect based on the following considerations. First, proteins with internal ribosome entry sites (IRES) that are not subject to EIF2α-mediated translation attenuation should be enriched relative to proteins without IRES in T_{ex} cells[34]. However, this was not the case (Extended Data Fig. 5a). Second, we did not observe enrichment of proteins that rely on the alternative translation initiation factor EIF2A owing to the presence of an unconventional 5′ upstream open reading frame[35] (Extended Data Fig. 5b). Third, proteins with concurrent upregulation at RNA and protein levels in T_{ex} cells were overrepresented in translation initiation, elongation and stress-response pathways (Extended Data Fig. 5c). Fourth, levels of the translation repressor PDCD4 (refs. 36,37) were significantly reduced in T_{ex} cells both in vitro and in vivo (Extended Data Fig. 5d). Fifth, our proteomic analysis revealed an upregulation of translation but not transcriptional machinery in T_{ex} cells (Extended Data Fig. 5e–g). Proteins involved in translation were upregulated in T_{ex} cells induced by chronic LCMV clone 13 infection (Extended Data Fig. 6a). Moreover, the translation initiation factors EIF2D and EIF4G3 exhibited sustained high expression in P14 cells from mice with chronic infection but were reduced over time in mice with acute infection (Extended Data Fig. 6b).

These findings prompted us to directly assess translation rates by measuring the incorporation of L-homopropargylglycine (HPG), a methionine analogue, into newly synthesized proteins. Notably, T_{ex} cells exhibited a significantly increased rate of protein synthesis compared with acutely stimulated T_{eff} cells (Fig. 2e). We also measured translation changes in vivo in different TIL subsets by injecting O-propargyl-puromycin (OPP) into mice with MC38 tumours to label elongating polypeptide chains during active translation[38]. T_{tex} cells showed significantly higher OPP incorporation than T_{prog} and T_{int} cells (Fig. 2f). We validated this result by isolating TILs into single-cell suspensions followed by ex vivo HPG translation assays. This experiment was performed to further exclude the possibility that different spatial distributions of T cell subpopulations caused inconsistent access to OPP. Consistently, T_{tex} cells showed increased protein translation rates in both MC38 and MB49 tumour models (Extended Data Fig. 6c,d).

Next, we characterized important subcellular events typically associated with PSR. Stress granules (SGs) are dynamic, reversible protein and RNA granules that form under cellular stress and are evident during T cell activation[39,40]. The formation of SGs in T_{ex} cells was increased, as evidenced by both analyses of morphology and expression of the SG marker G3BP1 (Extended Data Fig. 7a–c). We further explored the functional roles of SGs in T_{ex} cells. Disruption of SGs by knocking out *G3bp1* resulted in an increased production of the cytokines IFNγ and TNF (Extended Data Fig. 7d,e). However, loss of *G3bp1* significantly compromised the survival of chronically stimulated T_{ex} cells (Extended Data Fig. 7f).

T_{ex} cells also exhibited increased proteasome and lysosome activity (Extended Data Fig. 7g,h). We therefore investigated the kinetics of global protein catabolism in T_{ex} cells. Cells were labelled with HPG for 30 min, then changed to regular culture conditions without HPG. Although nascent proteins were produced in high levels, they were rapidly degraded in T_{ex} cells (Extended Data Fig. 7i). This protein catabolism in T_{ex} cells was driven largely by autophagy (Extended Data Fig. 7j).

Taken together, these results show that T_{ex} cells have a distinct non-canonical PSR, which we term T_{ex}-PSR. T_{ex}-PSR is characterized by the induction of PSR and the formation of SGs, protein aggregate accumulation and increased protein catabolism, coupled paradoxically by enhanced global protein synthesis.

Molecular definition of protein aggregates

We next asked what proteins were prone to aggregation in T_{ex} cells. To that end, we used native gel electrophoresis to analyse the migration pattern of proteomes (Fig. 2g). On the basis of proteome characterization, we focused on the following three differentiation states of T cells: T_{eff} cells (day 4 acutely activated T cells); early T_{ex} cells (day 4 chronically activated T cells); and late T_{ex} cells (day 8 chronically activated T cells) (Extended Data Fig. 4c,d). Both early and late T_{ex} cells showed upregulation of ER stress responses compared with T_{eff} cells (Extended Data Fig. 4e,f). To define aggregation-prone proteins, T_{eff}, early and late T_{ex} cells were first lysed with mild lysis buffer to maintain their native conformation followed by high-speed centrifugation to remove nucleoli and other insoluble materials. Supernatants were then subjected to native PAGE electrophoresis. Proteins that migrated below 140 kDa (low molecular weight (LMW) species) and above (high molecular weight (HMW) species) from the gel were then defined by MS. We detected and quantified 3,889 proteins, and 2,878 of these proteins (74%) shifted from LMW to HMW species in T_{ex} cells. This finding indicated that there was a large-scale level of protein aggregation in the exhaustion state (Fig. 2h). We next examined whether proteins associated with specific pathways were preferentially aggregated in T_{ex} cells. However, there was no such preference, which suggested that protein aggregation occurred globally (Fig. 2i). Still, effector molecules, including granzyme B, granzyme C and perforin, in T_{ex} cells showed significant enrichment in HMW species compared with T_{eff} cells (Fig. 2j). The T_{ex}-PSR chaperones gp96 and BiP also showed a trend in moving towards HMW species. Notably, AKT1 did not demonstrate signs of aggregation in T_{ex} cells (Fig. 2j). We also resuspended and profiled proteins in insoluble material through additional harsh lysis (Extended Data Fig. 8a). We observed an enrichment of granzyme B in T_{ex} cells compared with T_{eff} cells (Extended Data Fig. 8b). The inhibitory receptor PD1, despite being a transmembrane protein, was retained in the soluble fraction (Extended Data Fig. 8c).

Next, we used immunoblotting to validate the aggregation state of some of the identified proteins (Fig. 2k). In T_{ex} cells, granzyme B and perforin showed a migration pattern above 242 kDa, which was in contrast to T_{eff} cells (Fig. 2l,m). The T_{ex}-PSR chaperone gp96 also formed more abundant and distinct HMW species in T_{ex} cells, which was not the case with cytosolic HSP90α (Fig. 2l,m). The aggregation-prone proteins in T_{ex} cells were also enriched in the insoluble fraction (Fig. 2n). Taken together, these data indicate that protein quality control is severely compromised in T_{ex} cells, which showed a tendency of protein aggregation at the global level.

Misfolded proteins drive exhaustion

An important question is whether protein aggregation is the cause or a consequence of T cell exhaustion. We induced protein aggregation in T cells using two approaches and then programmed these cells under non-exhaustion conditions. First, we treated T_{eff} cells with the L-proline analogue L-azetidine-2-carboxylic acid (AZC) (Fig. 3a) to cause protein misfolding through the four-membered ring[41,42]. L-Proline was not

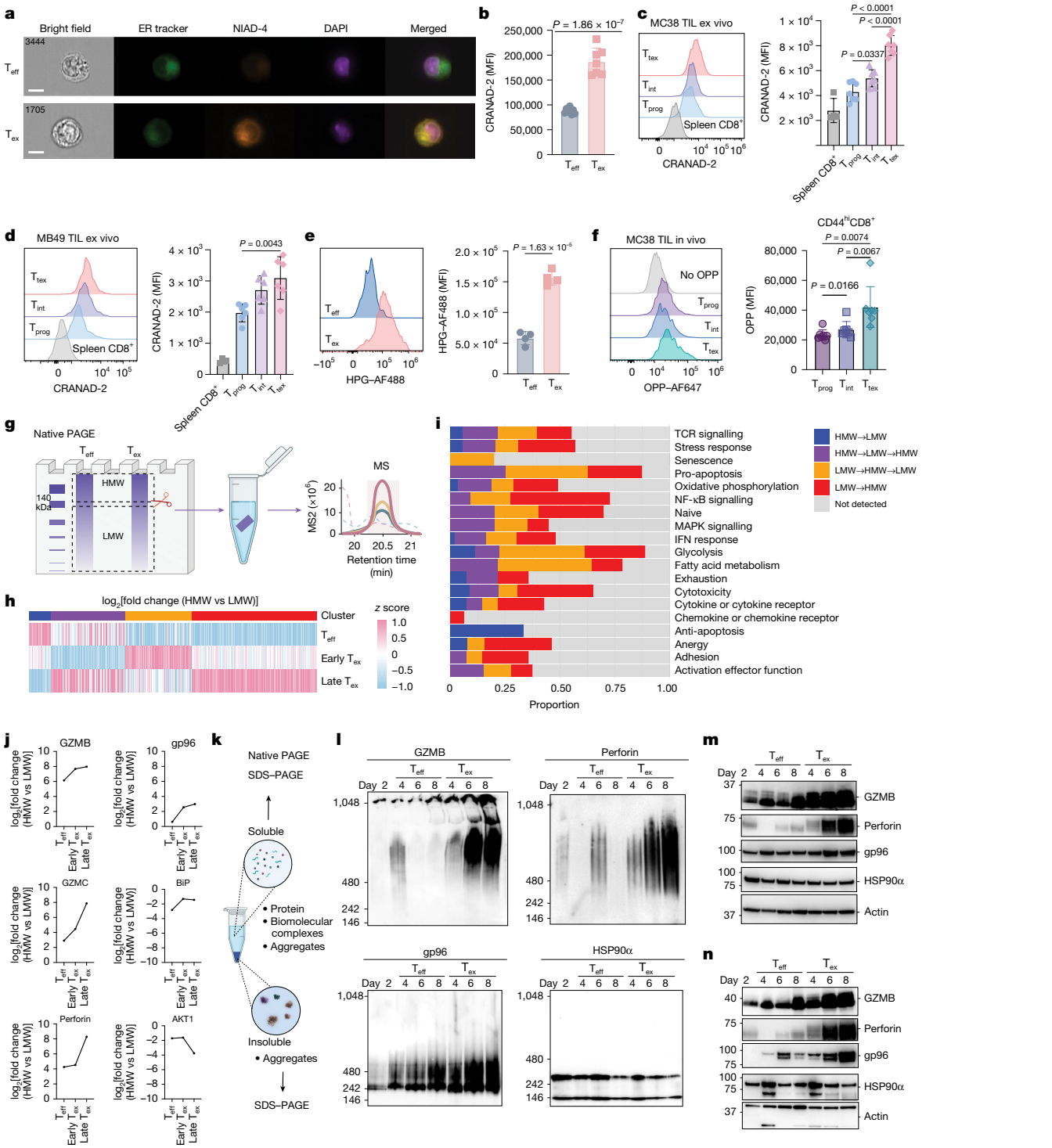

Fig. 2 | Chronic TCR stimulation disrupts proteostasis during T cell exhaustion. a, ImageStream analysis of protein aggregates in T_{eff} and T_{ex} cells 8 days after initial activation in vitro. Numbers are identifiers of representative cells within the samples. Scale bar, 7 µm. **b**, Flow cytometry quantification of protein aggregates ($n = 8$ for T_{eff} and $n = 7$ for T_{ex}, two-tailed t-test). MFI, mean fluorescence intensity. **c**,**d**, Protein aggregates in CD8$^+$ T cell subpopulations from mouse MC38 tumours (**c**) and MB49 tumours (**d**) ($n = 4$ for spleens, $n = 7$ for TILs, one-way analysis of variance (ANOVA)). **e**, Flow cytometry histogram and bar plot of HPG incorporation in T_{eff} and T_{ex} cells in vitro ($n = 4$, two-tailed t-test). **f**, Flow cytometry histogram and bar plot of OPP incorporation in CD8$^+$ T cell subpopulations from mouse MC38 tumours ($n = 7$, one-way ANOVA). **g**, Schematic of native PAGE and determination of the proteome by MS. T_{eff} and T_{ex} cells were generated as described in Extended Data Fig. 4d. **h**, Heatmap showing the fold change of 3,889 proteins in HMW and LMW species. **i**, Lack of association between aggregation tendency of proteins and their functional pathways. Bar colours depict the migration pattern of proteins as indicated in **h**. **j**, Fold changes of indicated protein abundances in HMW and LMW species. **k**, Schematic of cell lysate fractionation based on protein solubility. **l**, Immunoblot analysis of granzyme B (GZMB), perforin, gp96 and HSP90α in the soluble fractions of cell lysates separated by native PAGE. **m**, Immunoblot analysis of the indicated proteins in soluble fractions separated by SDS–PAGE. **n**, Immunoblot analysis of the indicated proteins in insoluble fractions resolved by SDS–PAGE. For **l**–**n**, the values on the left of the blots are kDa. For immunoblot source data, see Supplementary Fig. 1. Data in **h**–**j** are representative of two independent experiments. Experiments in **l**–**n** were repeated at least three times. Data are presented as the mean ± s.d. (**b**–**f**). The diagrams in **g** and **k** were created using BioRender (https://www.biorender.com).

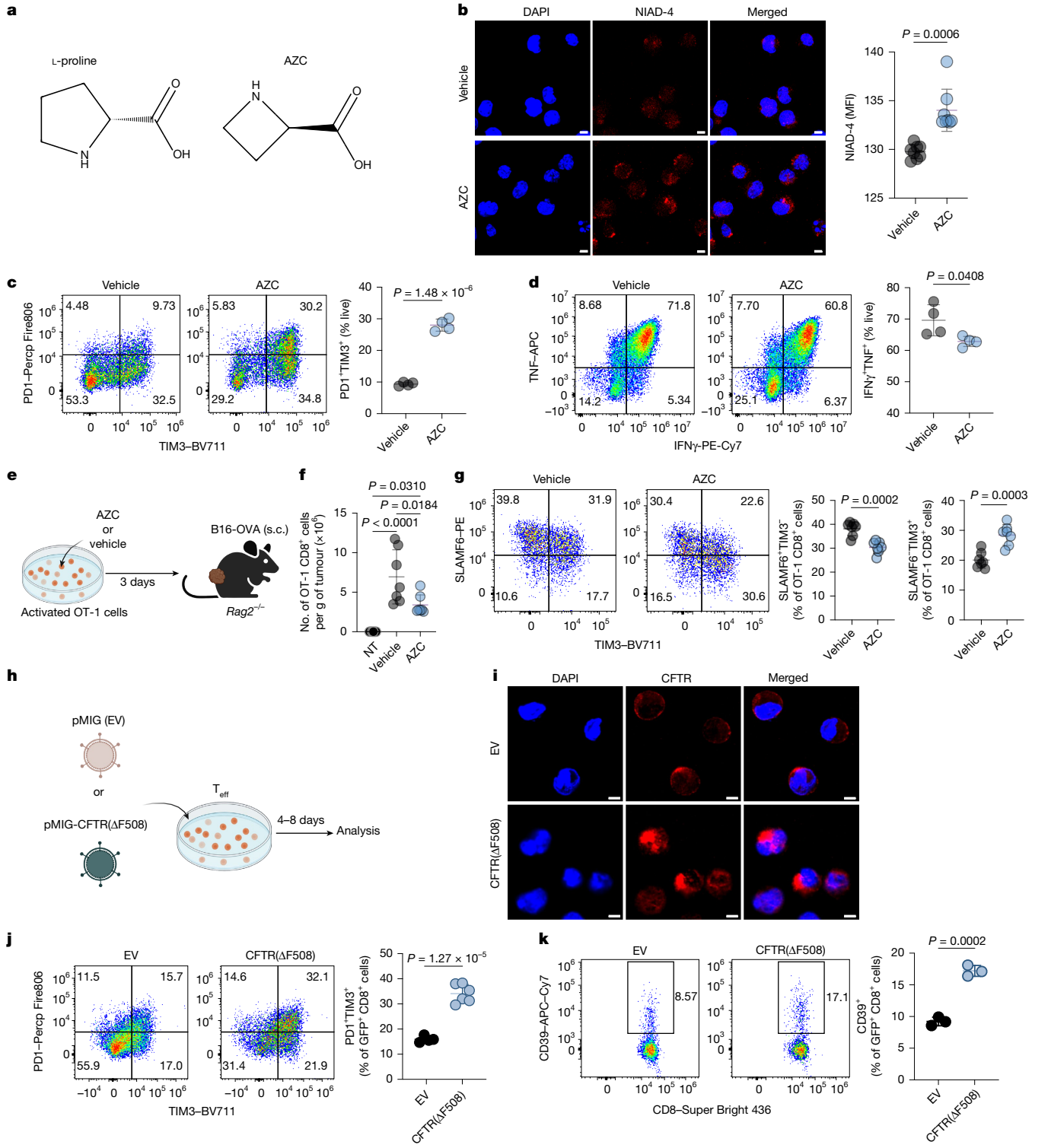

Fig. 3 | Protein misfolding promotes T cell exhaustion without chronic TCR stimulation. a, Structure of L-proline and its analogue AZC. **b**–**d**, Mouse T_{eff} cells were treated with AZC for 6 days in vitro 2 days after optimal activation. **b**, Confocal imaging analysis (left) and quantification (right) of protein aggregates ($n = 8$, two-tailed t-test. Experiments were repeated at least 3 times). Scale bars, 5 µm. **c**, Percentages of $PD1^+TIM3^+$ cells out of the total live $CD8^+$ T cells ($n = 4$, two-tailed t-test). **d**, Percentages of $IFN\gamma^+TNF^+$ cells over the total live $CD8^+$ T cells ($n = 4$, two-tailed t-test). **e**, Schematic of adoptive transfer of AZC-pulsed or vehicle-pulsed OT-1 cells into *Rag2*$^{-/-}$ mice with B16-OVA tumours. NT, no transfer. **f**, Absolute number of tumour-infiltrating OT-1 $CD8^+$ T cells normalized by tumour weight ($n = 6$ for NT and $n = 7$ for vehicle and AZC, one-way ANOVA). **g**, Percentages of $SLAMF6^+TIM3^-$ and $SLAMF6^-TIM3^+$ tumour-infiltrating OT-1 cells ($n = 7$, two-tailed t-test). **h**, Schematic of introducing a model aggregation-prone protein, CFTR(ΔF508), into T_{eff} cells by retrovirus transduction. **i**, Confocal imaging analysis of CFTR expression in cells transduced with CFTR(ΔF508) or empty vector (EV). Scale bars, 5 µm. **j**, Percentages of $PD1^+TIM3^+$ cells over total mouse $CD8^+$ T cells transduced with CFTR(ΔF508) or EV ($n = 4$ for EV and $n = 6$ for CFTR(ΔF508), two-tailed t-test). **k**, Percentages of $CD39^+$ cells out of the total transduced human $CD8^+$ T cells 10 days after transduction ($n = 3$, two-tailed t-test. Experiments were repeated 3 times with cells from different donors with similar results). Data are presented as the mean ± s.d. (**b**–**d**,**f**,**g**,**j**,**k**). The diagrams in **e** and **h** were created using BioRender (https://www.biorender.com).

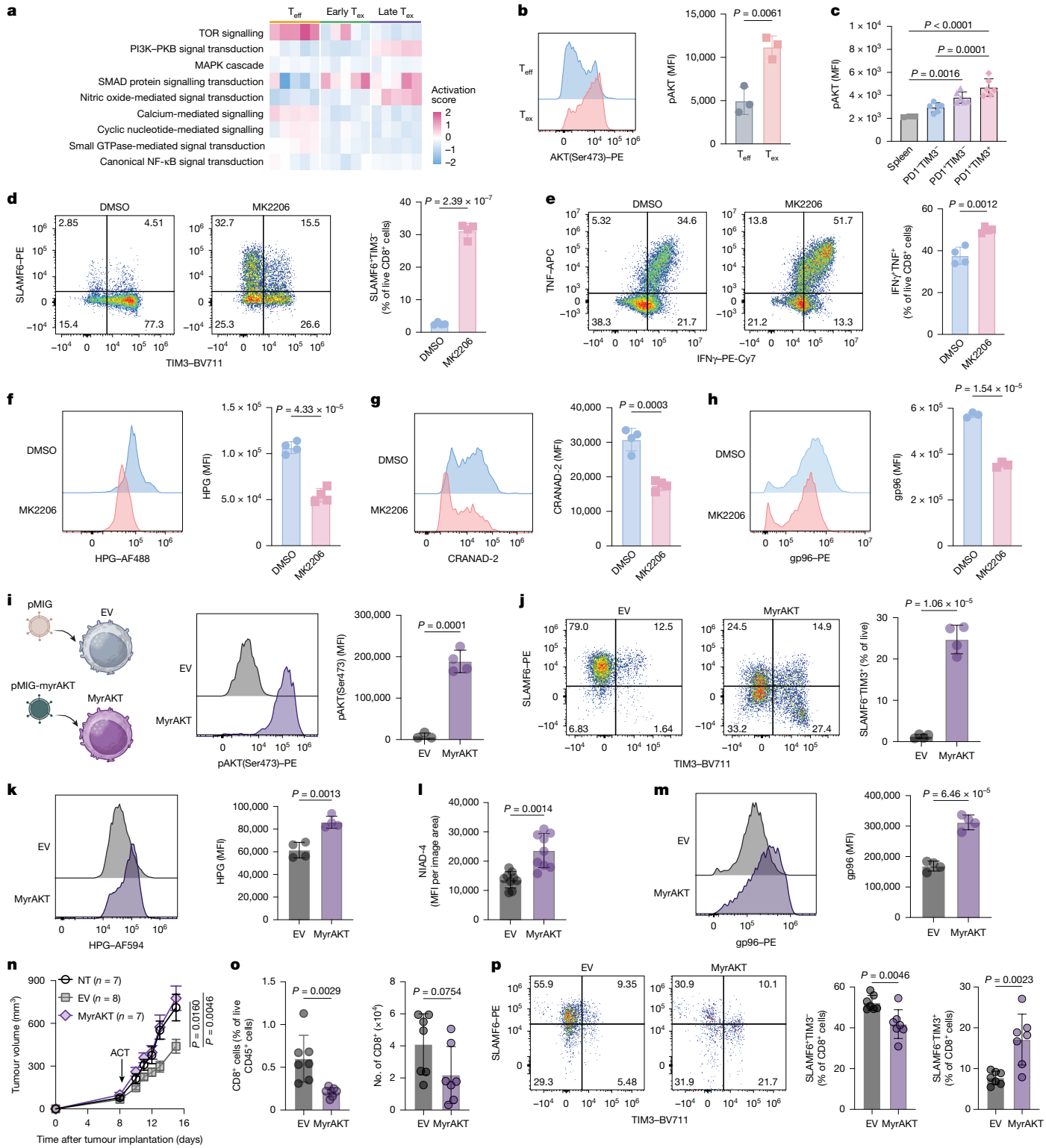

Fig. 4 | See next page for caption.

depleted in the culture medium to avoid metabolic disruption. After 6 days of treatment of T cells with AZC, apparent protein aggregation was observed (Fig. 3b). Despite culturing T cells in the non-exhaustion conditions, AZC treatment caused them to develop into the T_{ex} cell state, with a significantly increased $PD1^+TIM3^+$ population and impaired cytokine production (Fig. 3c,d). As expected, T_{ex} cells were vulnerable to AZC treatment, with significantly more cell death (data not shown). We also analysed AZC-treated cells in the tumour environment. OT-1 cells were activated and transiently pulsed with AZC for 3 days before adoptive transfer into mice with B16-OVA tumours (Fig. 3e). AZC-treated OT-1 cells showed reduced numbers in the tumours and an increased $SLAMF6^-TIM3^+$ T_{tex} population (Fig. 3f,g). Second, we genetically induced the expression of an aggregation-prone and functionally inert protein into acutely activated T cells by retroviral transduction (Fig. 3h). Cystic fibrosis transmembrane conductance regulator (CFTR) is an ion channel protein expressed primarily in epithelial cells, with

Fig. 4 | Sustained AKT signalling induces T_{ex}-PSR and underlies T cell exhaustion. a, Expression levels of proteins in major signalling pathways in T_{eff} and T_{ex} cells in vitro as described in Extended Data Fig. 4d. **b**, Levels of phosphorylated AKT (pAKT(Ser473)) in mouse T_{eff} and T_{ex} cells in vitro ($n = 3$). **c**, pAKT staining in splenic $CD8^+$ T cells and TIL subsets from MC38 tumours ($n = 3$ for spleen, $n = 6$ for TILs, one-way ANOVA). **d**, Percentages of $SLAMF6^+TIM3^-$ cells in T cells treated with chronic TCR stimulation together with MK2206 or dimethyl sulfoxide (DMSO) for 6 days ($n = 4$). **e**, Percentages of $IFN\gamma^+TNF^+$ cells after re-stimulation in T cells treated as in **d** and rested for 2 days ($n = 4$). **f**, Quantification of HPG incorporation in T cells treated as in **d** ($n = 4$). **g**, Quantification of protein aggregation in T cells treated as in **d** ($n = 4$). **h**, gp96 expression in T_{ex} cells treated with MK2206 for 2 days ($n = 3$). **i**, Schematic of packaging MSCV-GFP (pMIG) retrovirus expressing myrAKT for T cell transduction, and the flow cytometry quantification of pAKT(Ser473) in mouse T cells transduced with myrAKT or EV ($n = 3$ for EV, $n = 4$ for myrAKT). **j**–**m**, Quantification of $SLAMF6^-TIM3^+$ cells (**j**), HPG incorporation (**k**), protein aggregation by live-cell imaging (**l**) and gp96 expression (**m**) in T cells transduced with myrAKT or EV ($n = 4$ (**j**,**k**,**m**) or $n = 9$ (**l**) per group). **n**, Tumour growth curves (two-way ANOVA). OT-1 cells transduced with myrAKT or EV were transferred into *Rag2*$^{-/-}$ mice with B16-OVA tumours. **o**, Percentages and absolute number of OT-1 T cells transduced with myrAKT or EV from tumours 5 days after adoptive cell transfer (ACT) ($n = 7$). **p**, Percentages of $SLAMF6^+TIM3^-$ and $SLAMF6^-TIM3^+$ OT-1 cells from tumours ($n = 7$). Two-tailed *t*-test for comparisons between two groups. Data are the mean ± s.d. (**b**–**m**,**o**,**p**) or the mean ± s.e.m. (**n**). The diagram in **i** was created using BioRender (https://www.biorender.com).

low levels of expression in T lymphocytes[43]. Deletion of phenylalanine at the 508th position (CFTR(ΔF508)) in human CFTR leads to protein misfolding and ER retention[44,45]. Transduction of the folding-deficient mutant CFTR(ΔF508) resulted in the intracellular accumulation of CFTR aggregates in mouse $CD8^+$ T cells (Fig. 3i). Moreover, overexpression of CFTR(ΔF508) induced bona fide T cell exhaustion without repetitive TCR stimulation (Fig. 3j). CFTR(ΔF508) also increased $CD39^+$ populations in acutely activated human $CD8^+$ T cells (Fig. 3k). Together, these results suggest that protein aggregation has a causal role in T cell exhaustion.

Sustained AKT activity causes exhaustion

We next aimed to elucidate the upstream signalling hub that is responsible for mediating T_{ex}-PSR and promoting T cell exhaustion. We examined the expression level of components of key signalling pathways defined in the Gene Ontology database in our T cell proteome dataset. The AKT pathway was specifically upregulated in the late T_{ex} cell population (Fig. 4a). Flow cytometry analysis further showed that AKT phosphorylation was enhanced in T_{ex} cells (Fig. 4b). Chronic AKT signalling was also observed in T_{ex} cells isolated from MC38 tumours (Fig. 4c).

AKT often operates in the same signalling axis as PI3K and mTOR and has an important role in mediating T cell proliferation, survival and function[46,47]. Low-dose treatment with the AKT inhibitor MK2206 (0.2 μM and 1 μM) significantly increased the $SLAMF6^+TIM3^-$ population and cytokine production without impairing cell viability or proliferation (Fig. 4d,e and Extended Data Fig. 9a–d,f). However, treatment with the mTOR inhibitor rapamycin or the PI3K inhibitor LY294002 at any dose did not block T cell exhaustion, as indicated by the comparable proportion of $SLAMF6^+TIM3^-$ populations to the untreated group (Extended Data Fig. 9c). PI3K and mTOR inhibition also did not rescue cytokine production in T_{ex} cells (Extended Data Fig. 9d,f). All inhibitors directed cells to differentiate into the $CD44^+CD62L^+$ population, which validated that the dose levels used had pharmacological activities in chronically stimulated T cells (Extended Data Fig. 9e). We therefore focused on AKT in subsequent studies. Moderate attenuation of AKT signalling was sufficient to reduce the protein synthesis rate in T_{ex} cells and to reduce protein aggregation and T_{ex}-PSR chaperone gp96 expression (Fig. 4f–h). These results strongly suggest that AKT has a key role in driving T_{ex}-PSR and T cell exhaustion.

To further determine whether AKT signalling is the upstream driver of T_{ex}-PSR and T cell exhaustion, we expressed myristoylated AKT (myrAKT), a constitutively active form of AKT, in T cells[48,49] (Fig. 4i). MyrAKT expression converted T_{eff} cells into T_{ex} cells with a significant induction of $SLAMF6^-TIM3^+$ terminal exhausted phenotype under non-exhaustion conditions (Fig. 4j). This constitutively active AKT also upregulated protein translation, increased protein aggregation and induced the expression of the PSR chaperone gp96, which are all hallmarks of T_{ex}-PSR (Fig. 4k–m). To assess its functional impact, we transduced myrAKT into activated OT-1 cells and transferred them into mice with B16-OVA tumours. MyrAKT OT-1 T cells were no longer effective in controlling the growth of B16-OVA tumours in mice compared with wild-type (WT) OT-1 cells (Fig. 4n). MyrAKT-expressing T cells in the tumour microenvironment showed less tumour infiltration and more exhausted phenotypes compared with control T cells (Fig. 4o,p). We conclude that sustained AKT activation drives T_{ex}-PSR and T cell exhaustion.

T_{ex}-PSR chaperones underlie exhaustion

We next asked whether the T cell exhaustion program can be altered through the manipulation of T_{ex}-PSR chaperones. We initially selected ten genes that encode the following proteins that showed increased expression in T_{ex} cells and represent diverse molecular functions: ADAM8; annexin A2; cathepsin D (which is associated with cell death); ACADL (a fatty acid metabolic enzyme); the cytotoxic granzymes granzyme C and granzyme A; the temperature-sensitive channel protein TRPV2; and the three chaperone proteins BiP, gp96 and ERO1A (Extended Data Fig. 10a). The roles of these proteins on T cell exhaustion have not been previously defined. We knocked out these genes individually by CRISPR–Cas9 after T cell activation and then performed repetitive TCR stimulation. Gene deletion was confirmed by PCR with reverse transcription (RT–PCR) or flow cytometry (Extended Data Fig. 10b,c). Deleting each of the three chaperone genes *Hspa5*, *Hsp90b1* and *Ero1a* with single guide RNAs (sgRNAs sg*Hspa5*, sg*Hsp90b1* and sg*Ero1a*, respectively) significantly enhanced cytokine production, whereas individual knockout of the other seven genes had minimal effects (Fig. 5a and Extended Data Fig. 10d). Cells deficient in BiP, ERO1A or gp96 also showed increased SLAMF6 expression, along with reduced levels of TIM3 and CD39 (Extended Data Fig. 10e–g). Although chaperone proteins are responsible for facilitating protein folding, knocking out *Hsp90b1* resulted in the most significant reduction in protein aggregation, which indicated its potentially pivotal role in mediating T_{ex}-PSR-associated protein aggregate formation (Fig. 5b).

To validate whether *Hsp90b1* deletion has the same effect in counteracting T cell exhaustion in vivo, we generated $CD8^+$-specific *Hsp90b1* knockout (KO: *E8i-cre-Hsp90b1*$^{flox/flox}$) and knockdown (Het: *E8i-cre-Hsp90b1*$^{flox/WT}$, with 50% reduction in gp96 levels) mouse models, which were subjected to chronic LCMV clone 13 infection (Fig. 5c,d). Thirty days after infection, gp96 expression was upregulated in antigen-experienced $CD8^+$ T cells from WT mice, with T_{tex} cells demonstrating the highest level of expression (Extended Data Fig. 10h). *Hsp90b1* deletion resulted in a significant expansion of total and antigen-specific $CD8^+$ T cells in spleens (Fig. 5e). There was clear evidence of reprogramming of T cells after *Hsp90b1* deletion (Fig. 5f,g), with enrichment of $TCF1^+CX3CR1^-$ progenitor cells and $CX3CR1^+$ intermediate populations, along with reduced expression of TIM3 and CD39 (Fig. 5h,i).

Similarly, we assessed whether deleting chaperone *Hspa5* or *Ero1a* in P14 $CD8^+$ T cells improves their antitumour effect in a gp33-expressing MB49 tumour model (Fig. 5j). Mice receiving *Hspa5* or *Ero1a* KO P14 cells showed significantly better tumour control compared with those

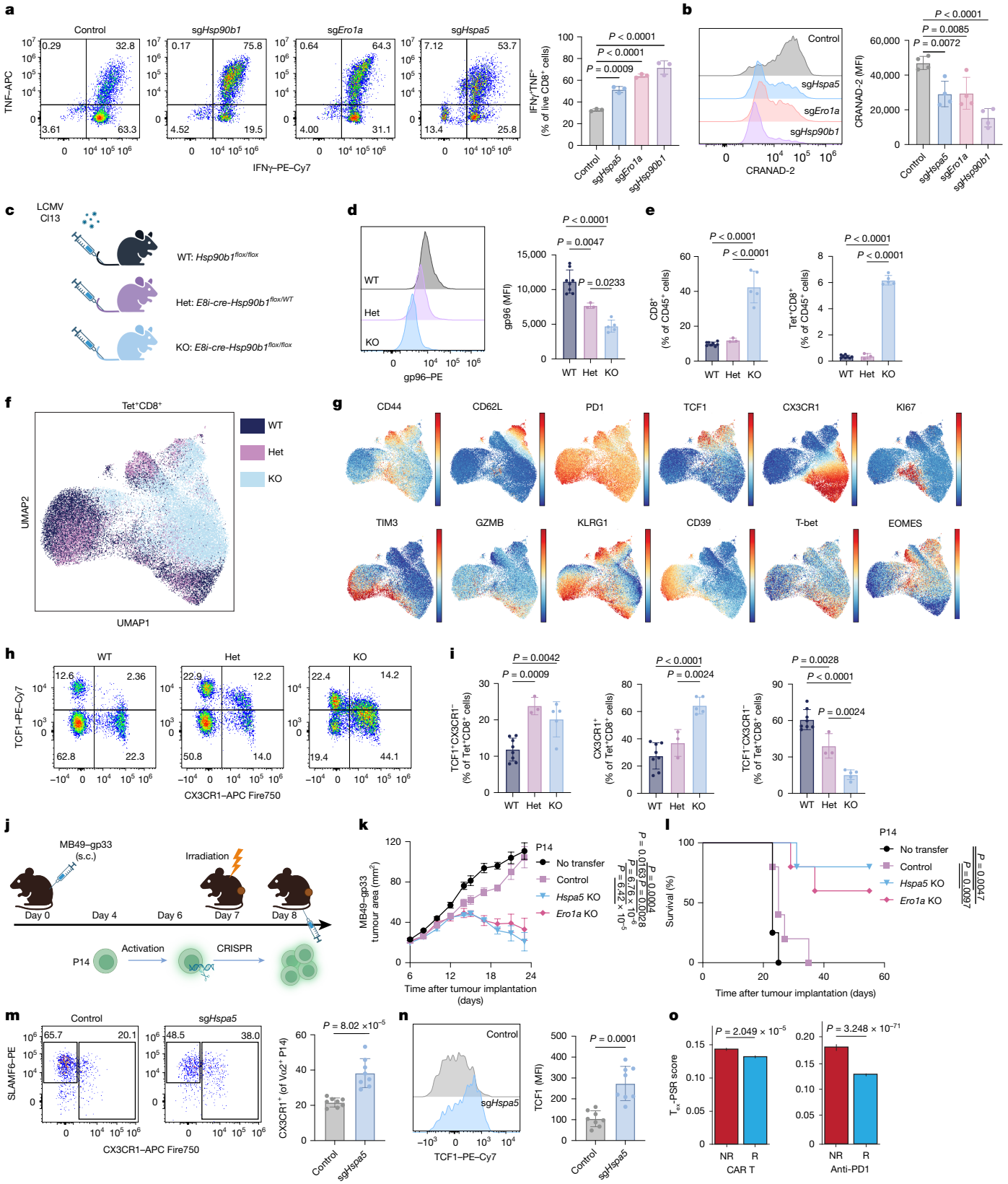

Fig. 5 | See next page for caption.

that received WT P14 cells (Fig. 5k,l). We also analysed the impact of BiP deficiency on P14 cells in the tumour microenvironment 5 days after adoptive transfer. BiP-null P14 T cells were more enriched in the cytolytic CX3CR1$^+$ population and showed improved stemness, as indicated by increased TCF1 expression, compared with WT cells (Fig. 5m,n). These data collectively suggest that targeting T_{ex}-PSR chaperones offer a potential approach for improving adoptive T cell transfer therapy for cancer.

Fig. 5 | Targeting T_{ex}-PSR chaperones prevents T cell exhaustion and enhances cancer immunotherapy. a, Frequencies of IFNγ$^+$TNF$^+$ cells ($n = 3$, one-way ANOVA) in cells with indicated genes knocked out. **b**, Quantification of protein aggregation by flow cytometry ($n = 4$, one-way ANOVA). **c**, Experimental scheme of using CD8$^+$ T cell-specific deletion of *Hsp90b1* in mice infected with LCMV clone 13. **d**, gp96 expression in total splenic CD8$^+$ T cells ($n = 8$ for WT, $n = 3$ for Het, $n = 5$ for KO, one-way ANOVA). **e**, Frequencies of total CD8$^+$ (left) and gp33-specific and gp276-specific (Tet$^+$) CD8$^+$ T cells (right) in spleens 30 days after infection ($n = 8$ for WT, $n = 3$ for Het, $n = 5$ for KO, one-way ANOVA). **f**, Uniform manifold approximation and projection (UMAP) of Tet$^+$ CD8$^+$ T cells profiled by 25-marker multispectral flow cytometry. **g**, Expression of selected markers mapped on UMAP. **h**,**i**, Representative flow cytometry (**h**) and quantification (**i**) of TCF1$^+$CX3CR1$^-$, CX3CR1$^+$ and TCF1$^-$CX3CR1$^-$ cells ($n = 8$ for WT, $n = 3$ for Het, $n = 5$ for KO, one-way ANOVA). **j**, Schematic of ACT using *Hspa5* KO, *Ero1a* KO or control cells. **k**, Tumour growth curves ($n = 4$ for NT, $n = 5$ for the other groups, two-way ANOVA). **l**, Kaplan–Meier survival curves ($n = 4$ for NT, $n = 5$ for the other groups, Mantel–Cox test). Results represent three independent experiments. **m**,**n**, Representative flow cytometry plots (left) and quantification (right) of CX3CR1$^+$ percentages (**m**) and TCF1 expression (**n**) in tumour-infiltrating P14 T cells 6 days after ACT ($n = 8$, two-tailed *t*-test). **o**, T_{ex}-PSR scores in scRNA-seq CD8$^+$ T cells from non-responders (NR) and responders (R) to anti-CD19 CAR T cell therapy for diffuse large B cell lymphoma[61] (left, NR: $n = 63{,}482$ cells from 57 patients; R: $n = 59{,}351$ cells from 52 patients) and anti-PD1 therapy for non-small cell lung cancer[62] and renal cell carcinoma (RCC)[63] (right, NR: $n = 5{,}672$ cells from 6 patients, R: $n = 37{,}884$ cells from 18 patients). Two-sided Wilcoxon rank-sum tests. Data are the mean ± s.d. (**a**,**b**,**d**,**e**,**i**,**m**,**n**) or mean ± s.e.m. (**k**,**o**). The diagrams in **c** and **j** were created using BioRender (https://www.biorender.com).

Clinical relevance of T_{ex}-PSR in cancer

Finally, we investigated the human relevance of T_{ex}-PSR in cancer. We performed pan-cancer CD8$^+$ T cell analyses with publicly available single-cell transcriptomic datasets that encompass 17 cancer types (Extended Data Fig. 11a). These T cells were isolated directly from samples taken from patients with cancer and did not have any other in vitro manipulations. To determine whether T_{ex}-PSR is also a feature of tumour-associated T_{ex} cells in humans, we generated a T_{ex}-PSR signature based on our in vivo and in vitro proteomic data (Extended Data Fig. 11b). The T_{ex}-PSR signature consisted of genes associated with proteostasis regulation that are concurrently upregulated in T_{ex} cells at the mRNA and protein levels (Extended Data Fig. 11c). The expression level of mRNAs encoding T_{ex}-PSR signature proteins was the highest in T_{tex} cells compared with all other T cell subsets from the tumour samples (Extended Data Fig. 11d). We also performed pseudotime trajectory analysis based on RNA velocity on pan-cancer CD8$^+$ T cells (Extended Data Fig. 11e). We observed two opposing differentiation trajectories: effector and exhaustion. The T_{ex}-PSR gene signature appeared early in the exhaustion trajectory, which increased proportionally as T cells become progressively exhausted (Extended Data Fig. 11f). By contrast, T_{ex}-PSR was significantly reduced during the effector trajectory. We analysed the T_{ex}-PSR score in CD8$^+$ T cells from patients with liver cancer. Patients with a lower T_{ex}-PSR signature in CD8$^+$ T cells showed better overall survival (Extended Data Fig. 11g). Moreover, a higher T_{ex}-PSR signature in patients with cancer also correlated with poor responses to immunotherapies, including both CAR T cells and ICBs (anti-PD1, and anti-PD1 with anti-CTLA4) (Fig. 5o and Extended Data Fig. 11h).

Discussion

The question of how protein quality control might differ between T cell activation and the exhaustion program has not been clearly answered. A key finding of our study was the activation of a distinct PSR in T_{ex} cells, which we term T_{ex}-PSR. This PSR is characterized by a high rate of protein translation, accumulation of SGs and global protein aggregation despite increased protein catabolism (Extended Data Fig. 12). The high translational rate in T_{ex} cells was not associated with the production of functional molecules. Our study provides an explanation to this paradox in that many proteins, such as granzymes and perforin, in T_{ex} cells aggregate instead of being properly folded, which may be a consequence of an overwhelmed protein quality control system. We also demonstrated that the introduction of misfolded proteins to T cells under optimal conditions for T_{eff} cell differentiation caused exhaustion. It has previously been reported[50] that tumour cells can evade T cell immunity by competing for methionine to alter T cell histone modifications. This result suggests that amino acid metabolism might have important roles in regulating T cell function by concurrently affecting translation and the epigenetic landscape[50]. Nonetheless, the causal relationship between PSR and T_{ex} suggests that dysregulated proteostasis can be a viable target for immunotherapeutic purposes. In this regard, it is worth noting that the HSP90 inhibitor ganetespib, which also inhibits the T_{ex}-PSR chaperone gp96, has been shown to promote ICB efficacy[51].

Our work identified AKT signalling as a central regulator of T_{ex}-PSR and T cell exhaustion. It is well established that PI3K–AKT–mTOR signalling is essential for T cell activation and differentiation by upregulating metabolic programs and supporting their bioenergetic needs[46,47]. However, the implications of AKT in T cell exhaustion are controversial and under-explored[52,53]. We demonstrated here that T_{ex} cells maintain chronic AKT signalling. Enforced expression of constitutively active AKT drives T_{ex}-PSR and a bona fide T cell exhaustion program. We therefore posit that AKT signalling is required for T cell survival, but its persistent activation disrupts the proteostatic equilibrium, which triggers T_{ex}-PSR and promotes exhaustion. Meanwhile, although often thought to operate on the same axis, mTOR inhibition by rapamycin did not show a substantial effect on preventing T cell exhaustion in our study. It may be because mTOR signalling is already suppressed in T_{ex} cells[47,52,54]. The plasticity of these signalling pathways suggests that the crosstalk of these signalling hubs in T cell exhaustion warrants further investigation.

Another intriguing aspect of T_{ex}-PSR activation in T_{ex} cells is the selective upregulation of T_{ex}-PSR chaperones. The role of T_{ex}-PSR chaperones presents a conundrum here in T_{ex} cells. Previous studies have reported that chaperones extend their impact beyond protein folding[55–58]. Moreover, AKT is a known client of HSP90 (ref. 59). Furthermore, ER chaperones such as BiP can translocate into the nucleus and function as TFs[60]. It is possible that the actions of T_{ex}-PSR chaperones in T_{ex} cells go beyond the fundamental role of protein folding and instead mediate signal transduction. An alternative and more simplistic explanation is that the chaperone machinery in T_{ex} cells is qualitatively suboptimal owing to the upregulation of some but not all chaperones. In T_{ex} cells, the T_{ex}-PSR chaperone stoichiometry is in disarray because of chaperone imbalance as well as substrate accumulation, which all result in pathological proteotoxic stress.

Under chronic stimulation, T cells must navigate a delicate balance between effector function and self-survival. We demonstrated that modulation of T_{ex}-PSR can enhance effector cytokine production at the expense of survival. Meanwhile, maintaining a high rate of protein synthesis might be advantageous for T_{ex} cells. This strategy ensures the production of essential proteins for their survival, albeit in a manner that is not cost-effective. Our study molecularly characterized the aggregation proteome. We demonstrated that protein aggregation in T_{ex} cells is a global event without selectivity, a result that highlights that it is the protein quality control machinery itself that is defective in T_{ex} cells. Our findings indicate that increased protein expression of T cell effector molecules per se without correcting the pathological T_{ex}-PSR in T_{ex} cells will not lead to functional improvement or reversal of the exhaustion phenotype. Moreover, we showed that the introduction of misfolded proteins alone, even in the absence of persistent

TCR stimulation, effectively induced a T cell exhaustion phenotype. Thus, the fate of T_{ex} cells is intricately linked to protein quality control. How T cells sense aggregates and subsequently reprogram T_{eff} cells to T_{ex} cells remains an open question that warrants further exploration.

Online content

Any methods, additional references, Nature Portfolio reporting summaries, source data, extended data, supplementary information, acknowledgements, peer review information; details of author contributions and competing interests; and statements of data and code availability are available at https://doi.org/10.1038/s41586-025-09539-1.

1. Zajac, A. J. et al. Viral immune evasion due to persistence of activated T cells without effector function. *J. Exp. Med.* **188**, 2205–2213 (1998).
2. Chow, A., Perica, K., Klebanoff, C. A. & Wolchok, J. D. Clinical implications of T cell exhaustion for cancer immunotherapy. *Nat. Rev. Clin. Oncol.* **19**, 775–790 (2022).
3. Wherry, E. J. T cell exhaustion. *Nat. Immunol.* **12**, 492–499 (2011).
4. Blank, C. U. et al. Defining 'T cell exhaustion'. *Nat. Rev. Immunol.* **19**, 665–674 (2019).
5. Hetz, C., Zhang, K. & Kaufman, R. J. Mechanisms, regulation and functions of the unfolded protein response. *Nat. Rev. Mol. Cell Biol.* **21**, 421–438 (2020).
6. Costa-Mattioli, M. & Walter, P. The integrated stress response: from mechanism to disease. *Science* https://doi.org/10.1126/science.aat5314 (2020).
7. McLane, L. M., Abdel-Hakeem, M. S. & Wherry, E. J. CD8 T cell exhaustion during chronic viral infection and cancer. *Annu. Rev. Immunol.* **37**, 457–495 (2019).
8. Hudson, W. H. et al. Proliferating transitory T cells with an effector-like transcriptional signature emerge from PD-1$^+$ stem-like CD8$^+$ T cells during chronic infection. *Immunity* **51**, 1043–1058 (2019).
9. Siddiqui, I. et al. Intratumoral Tcf1$^+$PD-1$^+$CD8$^+$ T cells with stem-like properties promote tumor control in response to vaccination and checkpoint blockade immunotherapy. *Immunity* **50**, 195–211 (2019).
10. Im, S. J. et al. Defining CD8$^+$ T cells that provide the proliferative burst after PD-1 therapy. *Nature* **537**, 417–421 (2016).
11. Miller, B. C. et al. Subsets of exhausted CD8$^+$ T cells differentially mediate tumor control and respond to checkpoint blockade. *Nat. Immunol.* **20**, 326–336 (2019).
12. Kurtulus, S. et al. Checkpoint blockade immunotherapy induces dynamic changes in PD-1$^-$CD8$^+$ tumor-infiltrating T cells. *Immunity* **50**, 181–194 (2019).
13. Schietinger, A. et al. Tumor-specific T cell dysfunction is a dynamic antigen-driven differentiation program initiated early during tumorigenesis. *Immunity* **45**, 389–401 (2016).
14. Lynn, R. C. et al. c-Jun overexpression in CAR T cells induces exhaustion resistance. *Nature* **576**, 293–300 (2019).
15. Chen, J. et al. NR4A transcription factors limit CAR T cell function in solid tumours. *Nature* **567**, 530–534 (2019).
16. Seo, H. et al. TOX and TOX2 transcription factors cooperate with NR4A transcription factors to impose CD8$^+$ T cell exhaustion. *Proc. Natl Acad. Sci. USA* **116**, 12410–12415 (2019).
17. Long, A. H. et al. 4-1BB costimulation ameliorates T cell exhaustion induced by tonic signaling of chimeric antigen receptors. *Nat. Med.* **21**, 581–590 (2015).
18. Vogel, C. & Marcotte, E. M. Insights into the regulation of protein abundance from proteomic and transcriptomic analyses. *Nat. Rev. Genet.* **13**, 227–232 (2012).
19. Schwanhausser, B. et al. Global quantification of mammalian gene expression control. *Nature* **473**, 337–342 (2011).
20. Maier, T., Guell, M. & Serrano, L. Correlation of mRNA and protein in complex biological samples. *FEBS Lett.* **583**, 3966–3973 (2009).
21. Jiang, L. et al. A quantitative proteome map of the human body. *Cell* **183**, 269–283 (2020).
22. Taniguchi, Y. et al. Quantifying *E. coli* proteome and transcriptome with single-molecule sensitivity in single cells. *Science* **329**, 533–538 (2010).
23. Hukelmann, J. L. et al. The cytotoxic T cell proteome and its shaping by the kinase mTOR. *Nat. Immunol.* **17**, 104–112 (2016).
24. Cuadrado, E. et al. Proteomic analyses of human regulatory T cells reveal adaptations in signaling pathways that protect cellular identity. *Immunity* **48**, 1046–1059 (2018).
25. Nicolet, B. P. & Wolkers, M. C. The relationship of mRNA with protein expression in CD8$^+$ T cells associates with gene class and gene characteristics. *PLoS ONE* **17**, e0276294 (2022).
26. Chang, C. H. et al. Posttranscriptional control of T cell effector function by aerobic glycolysis. *Cell* **153**, 1239–1251 (2013).
27. Vardhana, S. A. et al. Impaired mitochondrial oxidative phosphorylation limits the self-renewal of T cells exposed to persistent antigen. *Nat. Immunol.* **21**, 1022–1033 (2020).
28. Belk, J. A. et al. Genome-wide CRISPR screens of T cell exhaustion identify chromatin remodeling factors that limit T cell persistence. *Cancer Cell* **40**, 768–786 (2022).
29. Nusinow, D. P. et al. Quantitative proteomics of the Cancer Cell Line Encyclopedia. *Cell* **180**, 387–402 (2020).
30. Chu, Y. et al. Pan-cancer T cell atlas links a cellular stress response state to immunotherapy resistance. *Nat. Med.* **29**, 1550–1562 (2023).
31. Zander, R. et al. CD4$^+$ T cell help is required for the formation of a cytolytic CD8$^+$ T cell subset that protects against chronic infection and cancer. *Immunity* **51**, 1028–1042 (2019).
32. Beusch, C. M. et al. Longitudinal proteomic profiling of T cell differentiation in vivo unveils dynamic proteome remodeling. Preprint at *bioRxiv* https://doi.org/10.1101/2024.05.14.593504 (2024).
33. Nesterov, E. E. et al. In vivo optical imaging of amyloid aggregates in brain: design of fluorescent markers. *Angew. Chem. Int. Ed. Engl.* **44**, 5452–5456 (2005).
34. Gebauer, F. & Hentze, M. W. Molecular mechanisms of translational control. *Nat. Rev. Mol. Cell Biol.* **5**, 827–835 (2004).
35. Sendoel, A. et al. Translation from unconventional 5′ start sites drives tumour initiation. *Nature* **541**, 494–499 (2017).
36. Suzuki, C. et al. PDCD4 inhibits translation initiation by binding to eIF4A using both its MA3 domains. *Proc. Natl Acad. Sci. USA* **105**, 3274–3279 (2008).
37. Marchingo, J. M. & Cantrell, D. A. Protein synthesis, degradation, and energy metabolism in T cell immunity. *Cell. Mol. Immunol.* **19**, 303–315 (2022).
38. Signer, R. A., Magee, J. A., Salic, A. & Morrison, S. J. Haematopoietic stem cells require a highly regulated protein synthesis rate. *Nature* **509**, 49–54 (2014).
39. Franchini, D. M. et al. Microtubule-driven stress granule dynamics regulate inhibitory immune checkpoint expression in T cells. *Cell Rep.* **26**, 94–107 (2019).
40. Curdy, N. et al. The proteome and transcriptome of stress granules and P bodies during human T lymphocyte activation. *Cell Rep.* **42**, 112211 (2023).
41. Trotter, E. W. et al. Misfolded proteins are competent to mediate a subset of the responses to heat shock in *Saccharomyces cerevisiae*. *J. Biol. Chem.* **277**, 44817–44825 (2002).
42. Qian, S. B. et al. mTORC1 links protein quality and quantity control by sensing chaperone availability. *J. Biol. Chem.* **285**, 27385–27395 (2010).
43. Yoshimura, K. et al. Expression of the cystic fibrosis transmembrane conductance regulator gene in cells of non-epithelial origin. *Nucleic Acids Res.* **19**, 5417–5423 (1991).
44. Rommens, J. M. et al. Identification of the cystic fibrosis gene: chromosome walking and jumping. *Science* **245**, 1059–1065 (1989).
45. Riordan, J. R. CFTR function and prospects for therapy. *Annu. Rev. Biochem.* **77**, 701–726 (2008).
46. Chi, H. Regulation and function of mTOR signalling in T cell fate decisions. *Nat. Rev. Immunol.* **12**, 325–338 (2012).
47. Huang, H., Long, L., Zhou, P., Chapman, N. M. & Chi, H. mTOR signaling at the crossroads of environmental signals and T-cell fate decisions. *Immunol. Rev.* **295**, 15–38 (2020).
48. Pellman, D., Garber, E. A., Cross, F. R. & Hanafusa, H. An N-terminal peptide from p60src can direct myristylation and plasma membrane localization when fused to heterologous proteins. *Nature* **314**, 374–377 (1985).
49. Kharas, M. G. et al. Constitutively active AKT depletes hematopoietic stem cells and induces leukemia in mice. *Blood* **115**, 1406–1415 (2010).
50. Bian, Y. et al. Cancer SLC43A2 alters T cell methionine metabolism and histone methylation. *Nature* **585**, 277–282 (2020).
51. Mbofung, R. M. et al. HSP90 inhibition enhances cancer immunotherapy by upregulating interferon response genes. *Nat. Commun.* **8**, 451 (2017).
52. Staron, M. M. et al. The transcription factor FoxO1 sustains expression of the inhibitory receptor PD-1 and survival of antiviral CD8$^+$ T cells during chronic infection. *Immunity* **41**, 802–814 (2014).
53. Utzschneider, D. T. et al. Active maintenance of T cell memory in acute and chronic viral infection depends on continuous expression of FOXO1. *Cell Rep.* **22**, 3454–3467 (2018).
54. Ando, S. et al. mTOR regulates T cell exhaustion and PD-1-targeted immunotherapy response during chronic viral infection. *J. Clin. Invest.* https://doi.org/10.1172/JCI160025 (2023).
55. Liu, B. & Li, Z. Endoplasmic reticulum HSP90b1 (gp96, grp94) optimizes B-cell function via chaperoning integrin and TLR but not immunoglobulin. *Blood* **112**, 1223–1230 (2008).
56. Xu, Y. et al. Heat shock protein gp96 drives natural killer cell maturation and anti-tumor immunity by counteracting Trim28 to stabilize Eomes. *Nat. Commun.* **15**, 1106 (2024).
57. Zhang, Y. et al. GP96 is a GARP chaperone and controls regulatory T cell functions. *J. Clin. Invest.* **125**, 859–869 (2015).
58. Amankwah, Y. S. et al. Structural transitions modulate the chaperone activities of Grp94. *Proc. Natl Acad. Sci. USA* **121**, e2309326121 (2024).
59. Basso, A. D. et al. Akt forms an intracellular complex with heat shock protein 90 (Hsp90) and Cdc37 and is destabilized by inhibitors of Hsp90 function. *J. Biol. Chem.* **277**, 39858–39866 (2002).
60. Liu, Z. et al. ER chaperone GRP78/BiP translocates to the nucleus under stress and acts as a transcriptional regulator. *Proc. Natl Acad. Sci. USA* **120**, e2303448120 (2023).
61. Haradhvala, N. J. et al. Distinct cellular dynamics associated with response to CAR-T therapy for refractory B cell lymphoma. *Nat. Med.* **28**, 1848–1859 (2022).
62. Liu, B. et al. Temporal single-cell tracing reveals clonal revival and expansion of precursor exhausted T cells during anti-PD-1 therapy in lung cancer. *Nat. Cancer* **3**, 108–121 (2022).
63. Bi, K. et al. Tumor and immune reprogramming during immunotherapy in advanced renal cell carcinoma. *Cancer Cell* **39**, 649–661 (2021).

Methods

Cell lines

The MC38 cell line was purchased from Kerafast (ENH204-FP). The MB49 cell line was purchased from Sigma-Aldrich (SCC148). The HEK293T cell line was purchased from the American Type Culture Collection (CRL-3216). The MB49-gp33 cell line was shared by W. Cui (Northwestern University). The B16-OVA cell line was generated as previously described[64] and shared by L. Deng (Memorial Sloan Kettering Cancer Center). HEK293T, MC38 and MB49 cells were cultured in Dulbecco's modified Eagle medium (DMEM; Gibco, 11965-092) with 10% FBS (Gibco, 10082-147) and 1% penicillin–streptomycin (Gibco, 15140-122) at 37 °C and 5% CO_2. B16-OVA cells were cultured in RPMI-1640 (Gibco, 11875-093) with 10% FBS and 1% penicillin–streptomycin. Cell lines were regularly tested for mycoplasma contamination.

Mice

WT C57BL/6J mice (strain 000664) were purchased from The Jackson Laboratory. CD8-specific gp96-deficient mice were generated by crossing E8i-Cre mice (The Jackson Laboratory, strain 008766) and *Hsp90b1*$^{flox/flox}$ mice, previously generated and described by our group[65]. The P14 mouse strain was a gift from W. Cui (Northwestern University). OT-1 (strain 003831) and *Rag2*$^{-/-}$ (strain 033526) mice were purchased from The Jackson Laboratory. These mice were maintained in the animal facility at the Ohio State University under standard conditions (ambient temperature of 20–24 °C, relative humidity of 30–70% and a 12-h dark–light cycle (lights on from 6:00 to 18:00)). Mice aged 6–8 weeks were used for experiments. All procedures were performed in strict accordance with the recommendations in the Guide for the Care and Use of Laboratory Animals of the National Institutes of Health (NIH). The protocol was approved by the Committee on the Ethics of Animal Experiments of the Ohio State University.

T cell isolation, stimulation and drug treatment

Spleens were isolated from C57BL/6J mice and minced into single-cell suspensions. CD8$^+$ T cells were isolated using an immunomagnetic negative selection kit (Stemcell, 19853). Isolated CD8$^+$ T cells were first stimulated with 3 μg ml^{-1} plate-bound anti-CD3 (BioLegend, 100359) and 1 μg ml^{-1} anti-CD28 (BioLegend, 102121) antibodies in T cell medium made with RPMI-1640 with 10% FBS, 1% penicillin–streptomycin, 1 mM sodium pyruvate (Gibco, 11360-070), 1× MEM NEAA (Gibco, 11140-050), 10 mM HEPES (Gibco, 15630-080) and 50 μM 2-mercaptoethanol (Gibco, 21985-023) supplemented with 100 U ml^{-1} recombinant human IL-2 (acquired from the Biological Resources Branch at the NIH) in 12-well plates at a density of 10^6 cells per well for 48 h at 37 °C and 5% CO_2. For chronic stimulation, CD8$^+$ T cells were re-stimulated every 2 days by passaging to new plates with plate-bound anti-CD3 in T cell medium with IL-2. For acute stimulation, CD8$^+$ T cells were passaged every 2 days and maintained in T cell medium with IL-2. In some experiments, cells were treated with MK2206 (Cayman, 11593), LY294002 (Sigma-Aldrich, 440202) or rapamycin (Sigma-Aldrich, 553210) 2 days after initial activation and replenished concurrently with cell passage.

To measure cytokine production, activated cells were collected, plated and re-stimulated with 0.5× cell stimulation cocktail (Thermo Fisher, 00-4970-93) in T cell medium for 3 h at 37 °C and 5% CO_2.

Tumour challenge and TIL isolation

For the MC38 tumour model, 1×10^6 cells were subcutaneously injected into the right flank of shaved C57BL/6J mice. Mice were euthanized for tumour collection 16 days after tumour implantation for cell sorting. For the MB49 tumour model, 5×10^5 cells were subcutaneously injected into the right flank of shaved C57BL/6J mice. Tumours were collected 13 days after tumour implantation. To prepare single-cell suspensions, isolated tumours were chopped and washed with PBS before incubation with collagenase I (200 U ml^{-1}, Worthington, LS004196) in serum-free RPMI-1640 for 30 min at 37 °C with gentle agitation. After digestion, 2% BSA in PBS was added to cell suspensions to neutralize collagenase. Cell suspensions were washed with PBS and filtered through a 70 μm nylon filter. Single-cell suspensions were centrifuged and resuspended in PBS for downstream assays. For cell sorting, immune cells were enriched using a mouse TIL CD45 positive selection kit (Stemcell, 100-0350).

Flow cytometry

Cells were washed with PBS twice. Dead cells were stained using Live/Dead fixable blue (Invitrogen, L23105) or Zombie UV (BioLegend, 423108) at 4 °C for 15 min. Cells were washed with FACS buffer twice and a surface molecule staining antibody cocktail was applied for 30 min at 4 °C. After incubation, cells were washed twice with FACS buffer and then fixed and permeabilized using a FOXP3 fixation and permeabilization kit (eBioscience, 00-5523-00) overnight. After overnight fixation, cells were washed twice in permeabilization buffer and an intracellular staining antibody cocktail was added to the cells. After 2 h of incubation at room temperature, cells were washed twice with FACS buffer and analysed using Cytek Aurora. Acquired data were analysed with FlowJo software (v.10.10, BD Life Sciences) or OMIQ (Dotmatics) for high dimensional analysis. The gating strategy for TIL analysis is provided in Supplementary Fig. 2. A list of antibodies used for the multispectral flow cytometry study is provided in Supplementary Table 1.

For protein aggregation staining, cells were washed with HBSS (Sigma-Aldrich, H6648) twice and stained with 100 nM NIAD-4 (Cayman, 18520) or 50 μM CRANAD-2 (Cayman, 19814) in HBSS for 30 min at 37 °C and 5% CO_2. Cells were stained using Live/Dead fixable Near IR (Invitrogen, L34975) at 4 °C for 15 min, followed by fixation (BD Biosciences, 554655) for 15 min and DAPI staining for 5 min at room temperature. Cells were then analysed by ImageStream for acquiring fluorescent images or Cytek Aurora for quantification.

For SG analysis, cells were collected and stained using Live/Dead fixable NIR, followed by fixation in BD Cytofix fixation buffer (BD Biosciences, 554655) for 15 min and permeabilization using a FOXP3 fixation and permeabilization kit for 30 min at room temperature. Cells were then stained with anti-G3BP1 antibody (Proteintech, 13057-2-AP) in permeabilization buffer for 1 h at room temperature and then FITC-conjugated anti-rabbit antibody for 30 min. DAPI was added to the cell suspension and incubated for 5 min. Data were collected by ImageStream and analysed using IDEAS (v.6.2). Live cells were gated for SG analysis. Cells with SG loci were determined by gating on the Bight Detail Intensity feature high population on the FITC–G3BP1 channel.

Protein synthesis rate measurement

Nascent proteins were labelled using a Click-iT HPG Alexa Fluor 488 Protein Synthesis Assay kit (Thermo Fisher, C10428). Cells were incubated with 50 μM HPG (Thermo Fisher, C10186) in T cell medium made with methionine-free RPMI (Gibco, A14517-01) for 30 min at 37 °C and 5% CO_2. Cycloheximide (Sigma-Aldrich, 239763) was added to the negative control group at 50 μg ml^{-1} to inhibit translation. In some experiments, 2.5 μM MG132 (Sigma-Aldrich, M7449-1ML) or 10 nM bafilomycin A1 (Sigma-Aldrich, SML1661) was added to cells after HPG incubation. Cells were then labelled following the manufacturer's protocol and analysed using Cytek Aurora.

For measuring translation in TIL subsets in vivo, 50 mg kg^{-1} OPP (Vector Laboratories, CCT-1407-25) was administered into tumour-bearing mice by intraperitoneal injection. Mice were killed exactly 1 h after injection. Tumours were isolated and processed into single-cell suspensions. Cells were stained with surface markers and OPP was labelled using a Click-iT reaction kit following the manufacturer's protocol (Thermo Fisher, C10457).

Cell sorting

Single-cell suspensions were stained using Live/Dead fixable blue (Invitrogen, L23105) at 4 °C for 15 min. Cells were then washed twice

with FACS after viability dye staining. Tumour cells were enriched for $CD45^+$ lymphocytes using a mouse TIL positive selection kit (Stemcell, 100-0350) and spleen samples from mice infected with LCMV were enriched for $CD8^+$ T cells with a negative selection kit (Stemcell, 19853) before viability staining. Cells were then incubated with a surface staining antibody cocktail for 30 min at 4 °C. Cells were washed twice with FACS buffer and filtered through a 70 µm nylon filter immediately before loading into a Cytek Aurora CS for sorting. For sorting, a 100 µm nozzle was used for tumour-derived samples and a 70 µm nozzle for spleen-derived samples.

LCMV infection model

For acute LCMV infection, 8–10-week-old male mice were intraperitoneally inoculated with 2×10^5 p.f.u. LCMV Armstrong. For chronic LCMV infection, 8–10-week-old male mice were intravenously inoculated with 2×10^6 p.f.u. LCMV clone 13 in 400 µl RPMI-1640. Mice were euthanized on day 8 and day 30 after infection.

Gene editing in T cells by CRISPR–Cas9

The sgRNAs targeting each candidate were designed and purchased from IDT. The sequences of sgRNAs are provided in Supplementary Table 2. Two days before electroporation, splenic $CD8^+$ T cells were isolated and activated with 3 µg ml^{-1} plate-bound anti-CD3 and 1 µg ml^{-1} anti-CD28 antibodies in T cell medium supplemented with 100 U ml^{-1} IL-2. On the day of electroporation, RNPs were assembled by mixing 1.5 µl sgRNA and 1 µg Cas9 nuclease V3 (IDT, 1081059) and incubated at room temperature for 20 min. Electroporation was prepared using a P4 Primary Cell 4D-Nucleofector kit (Lonza, V4XP-4032). The activated T cells were washed with PBS twice and resuspended with P4 nucleofector solution with supplement provided by the kit. RNPs and 1 µl HDR Enhancer (IDT, 10007921) were added to the cell suspensions. The reaction mix was loaded into a Nucleocuvette after incubation at room temperature for 2 min. 4D-Nucleofector and program CMT137 were used for electroporation. Cells were rested in T cell medium with 50 U ml^{-1} IL-2 for 2 days and received re-stimulation every 2 days afterwards. At 8 days after electroporation, cells were collected for downstream analyses.

Protein electrophoresis and western blotting

Cells were pelleted and lysed in NP-40 buffer (50 mM Tris 7.4, 150 mM NaCl, 1% NP-40 and 0.1% sodium deoxycholate) supplemented with protease and phosphatase inhibitor cocktail (Thermo Fisher, 78440) and incubated on a roller for 30 min at 4 °C. Samples were centrifuged at 18,000*g*, 4 °C for 15 min and supernatant was transferred to fresh tubes as the detergent-soluble fraction. The detergent-insoluble fraction was resuspended in NP-40 buffer supplemented with 4% SDS. The protein concentration was quantified using a BCA assay (Pierce, 23227).

Native samples were diluted with native sample buffer (Thermo Fisher, NP) and run on 3–8% Tris-acetate gels (Thermo Fisher, EA0378) with Tris-glycine native running buffer (Thermo Fisher, LC2672). Samples were electrophoresed at 150 V for 3 h at 4 °C. SDS–PAGE samples were boiled in NuPAGE LDS sample buffer (Thermo Fisher, NP0007) and resolved on 4–12% Bis-Tris gels (Thermo Fisher, NP0335) with MOPS SDS running buffer (Thermo Fisher, NP0001). Samples were electrophoresed at 150 V for 1 h at room temperature. A list of antibodies used for western blot analyses is provided in Supplementary Table 1.

Retrovirus packaging and T cell transduction

The retroviral EV plasmid pMIG and pMIG-myrAKT were purchased from Addgene (52107, 65063). The open-reading frame for $CFTR^{\Delta F508}$ was synthesized and cloned into the pMIG plasmid for this study. To generate retrovirus for mouse T cell transduction, HEK293T cells were transfected with pMIG and pCL-Eco in Opti-MEM. The cell culture supernatant was collected 48 h after transfection and concentrated overnight with Retro-X Concentrator (Takara, 631456). Concentrated retrovirus was added onto plates coated with RetroNectin (Takara, T100B) and spun at 1,800*g* at 32 °C for 2 h. Virus supernatant was removed after centrifugation and washed with PBS twice. Polyclonal, P14 cells and OT-1 $CD8^+$ T cells that have been activated for 16–48 h were added to the virus-coated plate and cultured for 24 h. Cells were washed twice and plated into new plates for another 3–6 days for downstream analyses. For the generation of retrovirus for human T cell transduction, a similar approach to that used for mouse cells was used, with the key modification of using the Plat-A cell line for virus packaging. To transduce human $CD8^+$ T cells, $CD8^+$ T cells were magnetically isolated from peripheral blood mononuclear cells (Stemcell, 17953) and activated with Dynabeads (Gibco, 11131D) for 1 day. After activation, the cells were transduced with the indicated virus. In brief, the cells were spinoculated at 1,000*g* in a RetroNectin-virus-coated plate. After 24 h, the virus was removed, and subsequent analyses were performed after an additional 6–8 days of activation and maintenance.

ACT experiment

P14 cells were isolated from the spleens of P14 mice and activated with 1 µg ml^{-1} gp33 peptide. Two days after activation, cells were edited by CRISPR–Cas9 as described above and expanded for another 2 days with 100 U ml^{-1} IL-2. Next, 1×10^6 P14 cells were intravenously transferred per mouse. Then 5×10^5 MB49-gp33 cells were subcutaneously injected into the right flank of shaved WT C57BL/6J mice or *Rag2*$^{-/-}$ mice. WT mice were lymphodepleted using 5 Gray of total body irradiation on the day before cell transfer and randomized for treatment groups. OT-1 cells were activated and transduced with retroviral vector as described above. Transduced OT-1 cells were purified by cell sorting on the basis of positive GFP expression. In total, 2.5×10^5 OT-1 cells were intravenously transferred to B16-OVA tumour-bearing *Rag2*$^{-/-}$ mice. For OT-1 ACT experiments, 5×10^5 cells B16-OVA cells were subcutaneously injected into the right flank of *Rag2*$^{-/-}$ mice 8 days before adoptive transfer and randomized into treatment groups.

Immunofluorescence analysis by confocal microscopy

T cells were collected and spun onto glass coverslips in a 12-well plate. For protein aggregation staining, cells were stained with NIAD-4 and fixed as described above. For CFTR staining, cells were fixed with fixation buffer (BD, 554655) for 15 min, permeabilized with 0.5% Triton X-100 in PBS for 20 min and blocked with 2% BSA for 1 h. Cells were stained with primary anti-CFTR antibody (Proteintech, 20738-1-AP) and then Alexa Fluor 647-conjugated goat anti-rabbit IgG antibody (Thermo Fisher, A-21244). After staining, coverslips were mounted onto glass slides with mountant and DAPI (Thermo Fisher, P36962). Images were taken using an Olympus FV3000 microscope with ×60 magnification and processed with Olympus OlyVIA (v.4.2). For analysis, images were imported into ImageJ as .tiff files and adjusted to RGB stack format for downstream processing. Thresholds for positive detection of aggregates were determined through normalized autodetection and maintained across all images with a lower threshold of 100 and an upper threshold of 255 to generate binary image masks. The area, average size per particle, percentage of area and mean fluorescence intensity were analysed using the Analyze Particles function selected for area, area fraction, fluorescence intensity, particle count and average particle size.

MS sample processing

Cell samples were collected and washed with PBS once. Cell pellets were frozen at −80 °C if not immediately processed. Cells were lysed in lysis buffer made with 5% SDS (Thermo Fisher, AM9820), 50 mM TEAB (Thermo Fisher, 90114) and 2 mM $MgCl_2$ (Thermo Fisher, AM9530G) with HALT protease inhibitor cocktail (Thermo Fisher, 78441). Lysates were homogenized using either a probe sonicator or a Biorupter. DNA was removed by centrifugation at 13,000*g* for 10 min and the pellet discarded. For in vitro cell samples, the protein concentration was

quantified using a BCA assay (Pierce, 23227) and 50 µg protein of each sample was used for subsequent steps. For in vivo samples, total lysates were used assuming accurate FACS cell counts. Cell lysates were then treated with 20 mM DTT (Sigma-Aldrich, 10197777001) at 95 °C for 10 min, followed by the addition of 40 mM iodoacetamide (Pierce, A39271) at room temperature for 30 min in the dark and then quenched with 20 mM DTT for 15 min at room temperature. Phosphoric acid (1.2%; Sigma-Aldrich, 345245) was used to acidify proteins. Binding buffer with 100 mM TEAB in methanol (Thermo Fisher, A4581) was added to samples that were then loaded onto S-traps (ProtiFi, C01-micro-80) and washed with binding buffer 3 times. Proteins were digested with trypsin (Pierce, 90058) at 47 °C for 2 h. Digested peptides were eluted from S-traps with 0.2% formic acid (Thermo Fisher TS-28905) followed by a second elution with 50% acetonitrile (Sigma-Aldrich, T7408) in 0.2% formic acid. Eluates were pooled and lyophilized for storage at −80 °C.

MS acquisition

Peptides were reconstituted with 2% acetonitrile in 0.1% formic acid and separated using either an Easy-nLC 1200 coupled to an Thermo Exploris 480 tandem mass spectrometer (Thermo Fisher) or an UltiMate 3000 UHPLC coupled to a Thermo Fusion tandem mass spectrometer (Thermo Fisher). In both set ups, peptides were first desalted online using an Acclaim PepMap 100 Trap column (75 µm inner diameter, 150 mm length, 3 µm C18 packing) and then separated and ionized using either a 50 cm (Easy-nLC) or 25 cm (Ultimate 3000) Easy-Spray HPLC column (75 µm inner diameter, 2 µm C18 packing) with a 90-min linear gradient.

All data-independent acquisition (DIA) measurements were configured in a staggered window pattern using boundaries optimized to place window boundaries in forbidden zones. The Thermo Fusion was configured to use two DIA injections (covering peptide precursors from 400 to 700 *m/z* and from 700 to 1,000 *m/z*) of 38 ×8 *m/z*-wide windows in a staggered window pattern. These windows were configured to have 17,500 resolution and an automatic gain control (AGC) target of 4×10^5. Precursor spectra were placed every 38 scans (1 per cycle) using 35,000 resolution and an AGC target of 4×10^5. Similarly, the Thermo Exploris 480 was configured to use single-injection DIA measurements (covering peptide precursors from 400 to 1,000 *m/z*) of 38 × 16 *m/z*-width windows. These windows were configured to have 30,000 resolution and an AGC target of 1×10^6. Precursor spectra were placed every 38 scans (1 per cycle) using 60,000 resolution and an AGC target of 1×10^6.

For each dataset, a sample pool was made from subaliquots and used for library generation. We used gas-phase fractionation (GPF) DIA following the chromatogram library approach[66,67]. For this, we injected each peptide pool 6 times using different 100 *m/z* regions (400–500 *m/z*, 500–600 *m/z*, 600–700 *m/z*, 700–800 *m/z*, 800–900 *m/z* and 900–1,000 *m/z*). Each injection was configured to use 4 *m/z* staggered DIA windows and appropriate precursor windows. Otherwise, all measurements were performed as for normal DIA above on their respective instrument.

Proteomic data analysis

Raw files were demultiplexed using MSConvert in the Proteowizard package (v.3.0.20169)[68] and then searched using EncyclopeDIA (v.2.12.31). EncyclopeDIA was configured with the default settings for Orbitraps: 10 ppm precursor, fragment and library tolerances. EncyclopeDIA was allowed to consider both B and Y ions, and trypsin digestion was assumed. Searches were performed using a two-step procedure. First, the GPF-DIA injections were searched using a Prosit[69,70] predicted spectrum library to generate a chromatogram library based on the Mus musculus UniProt FASTA database (downloaded on 22 October 2019, containing 17,025 entries). All $z = +2$ or $z = +3$ peptides from 396.4 to 1002.7 *m/z* (with a maximum of one missed cleavage) were predicted assuming a normalized collision energy of 33. Peptides detected in the six GPF-DIA injections at a 1% peptide-level false discovery rate (FDR) were compiled into the chromatogram library. Quantitative DIA injections were searched against this chromatogram library, again filtered to a 1% peptide-level FDR. A normalized protein expression matrix for all proteomics generated in this study is provided in Supplementary Table 3. Bubble plots of protein expression were generated using the R package tidyverse (v.1.3.1)[71] based on *z* score-normalized protein expression values. Gene set enrichment analysis for protein clusters was performed using Enrichr[72–74].

Bulk RNA-seq sample preparation and data analysis

Acutely and chronically stimulated T cells were collected on day 8 after initial activation. Cells were washed with PBS twice and pelleted. RNA was first extracted using TRIzol and chloroform and then cleaned up using a RNeasy Micro kit (Qiagen, 74004). Sample library preparation and sequencing were performed by Azenta Life Sciences. Poly(A) selection was used for library preparation. Sequencing was performed using an Illumina NovaSeq platform with a depth of 50 million reads per sample. The raw bulk sequences were checked, trimmed and filtered using Fastp (v.0.23.4)[75]. The filtered reads were mapped to the mouse reference genome mm10 using HISAT2 (v.2.2.1)[76], and samtools (v.1.17)[77] was used to convert and sort BAM files. Last, the subread tool (v.2.0.6)[78] was used for gene quantification and generating the raw expression matrix. Raw expression data were first log-normalized, and the R package Limma (v.3.56.2)[79] was used to fit the model and perform differential expression analysis. To avoid NA values, a pseudo count of 1 was added to the raw count matrix. Genes with an absolute log[fold change] value greater than 1.5 and FDR-adjusted *P* value smaller than 0.05 are considered as differentially expressed genes.

Statistical comparison of protein expression and gene expression

To accurately compare protein and gene expression levels, we created a hash table (Supplementary Table 4) that included the protein accession number, protein name, gene name and Mouse Genome Informatics (MGI) number. Each protein and RNA matrix needed to match the hash table, and only the overlapped proteins and genes were kept.

We compared the normalized and log-transformed protein expression and gene expression levels in samples of the sample condition (for example, day 8 T_{ex} samples). Only proteins and genes that overlapped in both protein and RNA data were retained for comparison. A Pearson's correlation test was applied to calculate the correlation coefficient between protein expression and gene expression levels. We also compared the log[fold change] of proteins and genes between different conditions. The log[fold change] of proteins and genes were calculated in the analysis of differentially expressed genes described above.

We generated a functional gene list to further evaluate the expression level of proteins and genes undergoing specific cell functions, including 13 gene ontology terms, one EIF2A-dependent and one EIF2A-independent gene list. Specifically, the EIF2A-dependent and EIF2A-independent genes were determined according to the EIF2A-regulated upstream open reading frames[35]. As previously described[35], EIF2A-regulated upstream open reading frames were defined as the ratio of 5′ untranslated region (UTR) translation in control/5′ UTR translation in *Eif2a* KO > 4. The remaining mRNAs with a ratio <4 were defined as non-EIF2A regulated (EIF2A-independent). The 5′ UTR translation rate was quantified for mRNAs with an average of more than 16 reads over all replicates. Genes in each of the 26 lists are highlighted on the scatter plot to compare the protein and gene expression/log[fold change].

Gene signature score analysis

For each of the gene lists mentioned above, we also calculated a gene signature score based on the single-sample gene set enrichment analysis (ssGSEA) method. An in-house script was used to perform the ssGSEA analysis. The R package heatmaply (v.1.4.2)[80] or Morpheus

(https://software.broadinstitute.org/morpheus) was used to draw the heatmap. For gene signature score analysis for scRNA-seq data, the raw expression matrix of LCMV scRNA-seq data was downloaded from GSM3701181 (ref. 31). Cells were divided into three categories on the basis of gene expression levels: progenitor state (*Slamf6* > 0 and *Cx3cr1* = 0); intermediate state (*Cx3cr1* > 0); and terminal state (*Slamf6* = 0 and *Cx3cr1* = 0). Cells in each category were randomly divided into three equal subgroups. Pseudo bulk gene expression was defined by the average expression of genes in each cell subgroup. Then, the same ssGSEA method was performed on the pseudo bulk expression data to calculate the gene signature scores and to generate the heatmap.

Pan-cancer scRNA-seq data collection

To construct a comprehensive pan-cancer scRNA-seq dataset, we compiled transcriptomic profiles from 346 tumour samples derived from 251 individuals across 20 publicly available scRNA-seq datasets[81–100] (Supplementary Table 5). To ensure data consistency and to minimize platform-related biases, only datasets generated using the 10x Genomics droplet-based platform were included for our analyses.

Quality control and preprocessing of the pan-cancer scRNA-seq data. We applied rigorous quality control measures using the package Scanpy (v.1.9.5)[101] to filter and preprocess single-cell transcriptomic data. The following inclusion criteria were applied: (1) each cell expressed at least 200 genes; and (2) mitochondrial gene content remained below 20% of total counts. Further filtering steps removed the following data: (1) low-quality barcodes indicative of debris (<400 detected genes, <500 unique molecular identifiers); and (2) potential duplicate cells (>5,500 detected genes or >30,000 unique molecular identifiers). After quality control, raw count matrices and AnnData objects were concatenated, and counts were normalized to transcripts per million using sc.pp.normalize_total, followed by log-transformation with sc.pp.log1p. Non-tumour cells were excluded before normalization, which produced 1,030,968 high-quality single cells and 14,090 genes for downstream analyses.

Batch correction and data integration. To harmonize datasets across studies while preserving biological signals, we used the Python package scVI (scvi-tools v.1.0.4)[102] for batch-effect correction and data integration. The scVI model was trained with sample identity as a covariate, mitigating inter-sample technical variability while ensuring robust integration of multiple datasets. The efficiency of batch correction was assessed by quantifying the reduction in batch-specific effects while maintaining key biological variance. After correction, downstream analyses—including clustering, differential gene expression and trajectory inference—were performed on the integrated dataset. UMAP was used for visualization, depicting cellular heterogeneity across batches, datasets, sex, organ origins and cancer types.

Cell-type annotation of pan-cancer scRNA-seq data. To annotate cell populations, we leveraged the scANVI algorithm (scVI-tools v.1.0.4), which provided pre-labelled reference annotations for epithelial, endothelial, fibroblast, lymphoid, myeloid and plasma cells. Initial clustering was performed in the scANVI latent space, followed by Leiden clustering to assign cell identities. The scANVI model was trained with max_epochs=20, and cluster annotations were transferred with n_samples_per_label=100. For detailed characterization of T cell subpopulations, we further integrated corresponding AnnData objects and applied scVI-based batch correction.

Functional signature calculation for scRNA-seq data. We used the scanpy.tl.score_genes function from the Python package Scanpy (v.1.9.5) to compute gene set scores across individual cells, which enabled the quantification of functional signatures in the scRNA-seq dataset.

RNA velocity and trajectory inference

RNA velocity analysis was performed to infer the directionality of cellular state transitions using spliced and unspliced transcript counts. Velocities were computed using the scVelo toolkit (v.0.3.3)[103,104], which estimates transcriptional dynamics across single cells. The resulting velocity vectors were projected onto the UMAP embedding to visualize the flow of differentiation. To infer developmental trajectories, the Slingshot algorithm was applied to the UMAP coordinates, incorporating RNA velocity information to identify lineage structures. Slingshot fit smooth curves (principal curves) through the data and assigned pseudotime values along each inferred lineage. Two dominant lineages were identified: one progressing towards a T_{ex} cell phenotype (lineage 1) and the other towards an effector-like phenotype (lineage 2). Signature scores for naive, exhaustion and T_{ex}-PSR gene modules were calculated across pseudotime for each lineage using averaged normalized expression of predefined marker genes.

Validation of the T_{ex}-PSR signature in $CD8^+$ T cells and its prognostic impact

To assess the clinical significance of the T_{ex}-PSR signature in $CD8^+$ T cells, we analysed public processed scRNA-seq data from 116 liver cancer samples obtained from 94 male patients[105]. Survival analyses were restricted to primary tumours and metastatic samples. After quality filtering, batch correction and cell-type annotation using the established preprocessing pipeline, $CD8^+$ T cells were isolated and T_{ex}-PSR signature scores were computed using the scanpy.tl.score_genes function from the Scanpy package (v.1.9.5).

T_{ex}-PSR signature expression in $CD8^+$ T cells and its impact on patient survival. To evaluate the prognostic significance of T_{ex}-PSR expression levels in $CD8^+$ T cells, we performed survival analyses using Kaplan–Meier curves, with statistical comparisons conducted using the log-rank test and univariate Cox proportional hazards (Cox PH) models, as specified in each figure. Two additional multivariable Cox PH models were fitted to account for potential confounders. The hazard ratio and 95% confidence intervals were reported on the basis of these models. Kaplan–Meier survival curves were generated to compare high versus low T_{ex}-PSR expression in liver cancer scRNA-seq datasets, with *P* values computed using univariate Cox PH models. To determine the optimal cut-off value for T_{ex}-PSR signature expression in relation to survival outcomes, we used the surv_cutpoint function from the R package survminer. This approach uses maximally selected rank statistics from the R package maxstat[106] to stratify patients into low-risk and high-risk groups. Moreover, continuous variables included in the Cox PH[107] models were assessed for linearity to ensure model validity.

T_{ex}-PSR expression in immunotherapy-treated patients

We further investigated T_{ex}-PSR expression in responders and non-responders across independent scRNA-seq datasets from patients receiving diverse immunotherapy treatments, including CAR T cell therapy for refractory B cell lymphoma[61], anti-PD1 therapy for lung cancer and advanced renal cell RCC[62,63], and anti-CTLA-4 with anti-PD1 combination therapy for RCC[64,108]. For each dataset, we applied the same preprocessing pipeline, including quality filtering, batch correction and cell-type annotation, as described for the pan-cancer scRNA-seq dataset.

Statistical analysis

Statistical analyses were performed using GraphPad Prism (v.10). Two-tailed unpaired Student's *t*-test was used for comparison between two groups. One-way ANOVA was used for comparisons among three or more groups. Two-way ANOVA was used to compare curves of time-course studies, including cell and tumour growth curves. $P < 0.05$ was considered significant.

Reporting summary

Further information on research design is available in the Nature Portfolio Reporting Summary linked to this article.

Data availability

Proteomic data are available from the MassIVE repository (MSV000098609) and through ProteomeXchange (PXD066433). Normalized protein expression data are provided in Supplementary Table 3. Bulk RNA-seq data from this paper have been deposited into the NCBI Gene Expression Omnibus database with the identifier GSE303401. Source data are provided with this paper.

Code availability

Scripts generated for analysis are available from Zenodo (https://doi.org/10.5281/zenodo.16323779)[109].

64. Budhu, S. et al. Blockade of surface-bound TGF-β on regulatory T cells abrogates suppression of effector T cell function in the tumor microenvironment. *Sci. Signal.* **10**, eaak9702 (2017).
65. Yang, Y. et al. Heat shock protein gp96 is a master chaperone for Toll-like receptors and is important in the innate function of macrophages. *Immunity* **26**, 215–226 (2007).
66. Pino, L. K., Just, S. C., MacCoss, M. J. & Searle, B. C. Acquiring and analyzing data independent acquisition proteomics experiments without spectrum libraries. *Mol. Cell. Proteomics* **19**, 1088–1103 (2020).
67. Searle, B. C. et al. Chromatogram libraries improve peptide detection and quantification by data independent acquisition mass spectrometry. *Nat. Commun.* **9**, 5128 (2018).
68. Chambers, M. C. et al. A cross-platform toolkit for mass spectrometry and proteomics. *Nat. Biotechnol.* **30**, 918–920 (2012).
69. Gessulat, S. et al. Prosit: proteome-wide prediction of peptide tandem mass spectra by deep learning. *Nat. Methods* **16**, 509–518 (2019).
70. Searle, B. C. et al. Generating high quality libraries for DIA MS with empirically corrected peptide predictions. *Nat. Commun.* **11**, 1548 (2020).
71. Wickham, H. et al. Welcome to the Tidyverse. *J. Open Source Softw.* **4**, 1686 (2019).
72. Chen, E. Y. et al. Enrichr: interactive and collaborative HTML5 gene list enrichment analysis tool. *BMC Bioinformatics* **14**, 128 (2013).
73. Kuleshov, M. V. et al. Enrichr: a comprehensive gene set enrichment analysis web server 2016 update. *Nucleic Acids Res.* **44**, W90–W97 (2016).
74. Xie, Z. et al. Gene set knowledge discovery with Enrichr. *Curr. Protoc.* **1**, e90 (2021).
75. Chen, S., Zhou, Y., Chen, Y. & Gu, J. fastp: an ultra-fast all-in-one FASTQ preprocessor. *Bioinformatics* **34**, i884–i890 (2018).
76. Kim, D., Paggi, J. M., Park, C., Bennett, C. & Salzberg, S. L. Graph-based genome alignment and genotyping with HISAT2 and HISAT-genotype. *Nat. Biotechnol.* **37**, 907–915 (2019).
77. Li, H. et al. The Sequence Alignment/Map format and SAMtools. *Bioinformatics* **25**, 2078–2079 (2009).
78. Liao, Y., Smyth, G. K. & Shi, W. The Subread aligner: fast, accurate and scalable read mapping by seed-and-vote. *Nucleic Acids Res.* **41**, e108 (2013).
79. Ritchie, M. E. et al. limma powers differential expression analyses for RNA-sequencing and microarray studies. *Nucleic Acids Res.* **43**, e47 (2015).
80. Galili, T., O'Callaghan, A., Sidi, J. & Sievert, C. heatmaply: an R package for creating interactive cluster heatmaps for online publishing. *Bioinformatics* **34**, 1600–1602 (2018).
81. Li, R. Y. et al. Mapping single-cell transcriptomes in the intra-tumoral and associated territories of kidney cancer. *Cancer Cell* **40**, 1583–1599 (2022).
82. Zhang, Y. P. et al. Single-cell analyses of renal cell cancers reveal insights into tumor microenvironment, cell of origin, and therapy response. *Proc. Natl Acad. Sci. USA* **118**, e2103240118 (2021).
83. Werba, G. et al. Single-cell RNA sequencing reveals the effects of chemotherapy on human pancreatic adenocarcinoma and its tumor microenvironment. *Nat. Commun.* **14**, 797 (2023).
84. Ma, L. C. et al. Tumor cell biodiversity drives microenvironmental reprogramming in liver cancer. *Cancer Cell* **36**, 418–430 (2019).
85. Regner, M. J. et al. A multi-omic single-cell landscape of human gynecologic malignancies. *Mol. Cell* **81**, 4924–4941 (2021).
86. Chen, Y. P. et al. Single-cell transcriptomics reveals regulators underlying immune cell diversity and immune subtypes associated with prognosis in nasopharyngeal carcinoma. *Cell Res.* **30**, 1024–1042 (2020).
87. Xu, J. F. et al. Single-cell RNA sequencing reveals the tissue architecture in human high-grade serous ovarian cancer. *Clin. Cancer Res.* **28**, 3590–3602 (2022).
88. Li, C. B. et al. Single-cell transcriptomics reveals cellular heterogeneity and molecular stratification of cervical cancer. *Commun. Biol.* **5**, 1208 (2022).
89. Luo, H. et al. Pan-cancer single-cell analysis reveals the heterogeneity and plasticity of cancer-associated fibroblasts in the tumor microenvironment. *Nat. Commun.* **13**, 6619 (2022).
90. Sathe, A. et al. Single-cell genomic characterization reveals the cellular reprogramming of the gastric tumor microenvironment. *Clin. Cancer Res.* **26**, 2640–2653 (2020).
91. Kim, N. et al. Single-cell RNA sequencing demonstrates the molecular and cellular reprogramming of metastatic lung adenocarcinoma. *Nat. Commun.* **11**, 2285 (2020).
92. Lambrechts, D. et al. Phenotype molding of stromal cells in the lung tumor microenvironment. *Nat. Med.* **24**, 1277–1289 (2018).
93. Chen, S. J. et al. Single-cell analysis reveals transcriptomic remodellings in distinct cell types that contribute to human prostate cancer progression. *Nat. Cell Biol.* **23**, 87–98 (2021).
94. Ma, X. S. et al. Identification of a distinct luminal subgroup diagnosing and stratifying early stage prostate cancer by tissue-based single-cell RNA sequencing. *Mol. Cancer* **19**, 147 (2020).
95. Luo, H. et al. Characterizing dedifferentiation of thyroid cancer by integrated analysis. *Sci. Adv.* **7**, eabf3657 (2021).
96. Chen, Z. H. et al. Single-cell RNA sequencing highlights the role of inflammatory cancer-associated fibroblasts in bladder urothelial carcinoma. *Nat. Commun.* **11**, 5077 (2020).
97. Qian, J. B. et al. A pan-cancer blueprint of the heterogeneous tumor microenvironment revealed by single-cell profiling. *Cell Res.* **30**, 745–762 (2020).
98. Zhang, M. et al. Single-cell transcriptomic architecture and intercellular crosstalk of human intrahepatic cholangiocarcinoma. *J. Hepatol.* **73**, 1118–1130 (2020).
99. Peng, J. Y. et al. Single-cell RNA-seq highlights intra-tumoral heterogeneity and malignant progression in pancreatic ductal adenocarcinoma. *Cell Res.* **29**, 725–738 (2019).
100. Lin, W. et al. Single-cell transcriptome analysis of tumor and stromal compartments of pancreatic ductal adenocarcinoma primary tumors and metastatic lesions. *Genome Med.* **12**, 80 (2020).
101. Wolf, F. A., Angerer, P. & Theis, F. J. SCANPY: large-scale single-cell gene expression data analysis. *Genome Biol.* **19**, 15 (2018).
102. Gayoso, A. et al. A Python library for probabilistic analysis of single-cell omics data. *Nat. Biotechnol.* **40**, 163–166 (2022).
103. Bergen, V., Lange, M., Peidli, S., Wolf, F. A. & Theis, F. J. Generalizing RNA velocity to transient cell states through dynamical modeling. *Nat. Biotechnol.* **38**, 1408–1414 (2020).
104. Weiler, P., Lange, M., Klein, M., Pe'er, D. & Theis, F. CellRank 2: unified fate mapping in multiview single-cell data. *Nat. Methods* **21**, 1196–1205 (2024).
105. Xue, R. et al. Liver tumour immune microenvironment subtypes and neutrophil heterogeneity. *Nature* **612**, 141–147 (2022).
106. Lausen, B. & Schumacher, M. Maximally selected rank statistics. *Biometrics* **48**, 73–85 (1992).
107. Grambsch, P. M. & Therneau, T. M. Proportional hazards tests and diagnostics based on weighted residuals. *Biometrika* **81**, 515–526 (1994).
108. Krishna, C. et al. Single-cell sequencing links multiregional immune landscapes and tissue-resident T cells in ccRCC to tumor topology and therapy efficacy. *Cancer Cell* **39**, 662–677 (2021).
109. Wu, W. Proteostatic stress response drives T cell exhaustion and immune evasion. *Zenodo* https://doi.org/10.5281/zenodo.16323779 (2025).

Acknowledgements We thank K. Weller and B. McElwain for assisting with cell sorting and ImageStream analysis; Y. Koguchi, K. Reynolds and R. Davenport, J. Li and J. Jin for technical support; and all members of the Z.L. Laboratory and the Pelotonia Institute for Immuno-Oncology (PIIO) for discussions throughout the course of the study. This work was supported by NIH grants R01CA262069 (Z.L.), R01CA282501 (Z.L.), R35GM150723 (B.C.S.), R21CA267394 (B.C.S.) and R01AI170926 (H.E.G.). M.S.A., D.E.G. and C.M.B. were supported by an Emory MP3 Seed Grant (121861), a Winship Cancer Center Invest$ Pilot Award (147150) and a Swedish Research Council grant (2023-00510), respectively.

Author contributions Z.L., B.C.S. and Y.W. conceived the project, designed the experiments and wrote the paper with input from the rest of the authors. Y.W. was involved in all aspects of this study, including performing experiments, data analyses and interpretation. B.C.S. led the MS-based proteomic study. B.C.S., A.E.S. and G.G. performed liquid chromatography and tandem MS data acquisition and analyses. A.M., W.W., A.E.S. and B.C.S. performed bioinformatic analysis on the proteomic data and bulk RNA-seq data. X.C. performed pan-cancer scRNA-seq dataset collection and analyses. A.A.S., A.Y., T.X., G.X. and H.E.G. performed LCMV infection experiments. C.M.B., A.S.D., D.E.G. and M.S.A.-H. performed additional proteomic analyses on LCMV model data. N.-J.S., Y.S.A., M.V., J.K.M. and Z.W. assisted in performing experiments and manuscript preparation. H.W., S.C.-C.H. and R.W. assisted in data interpretation and manuscript preparation. Z.L. provided overall supervision of the study.

Competing interests Z.L. serves as a member of the scientific advisory board for HanchorBio. B.C.S. is a founder and shareholder in Proteome Software, which operates in the field of proteomics. No conflicts of interest were disclosed by the other authors.

Additional information

Supplementary information The online version contains supplementary material available at https://doi.org/10.1038/s41586-025-09539-1.

Correspondence and requests for materials should be addressed to Zihai Li.

Peer review information *Nature* thanks the anonymous reviewer(s) for their contribution to the peer review of this work.

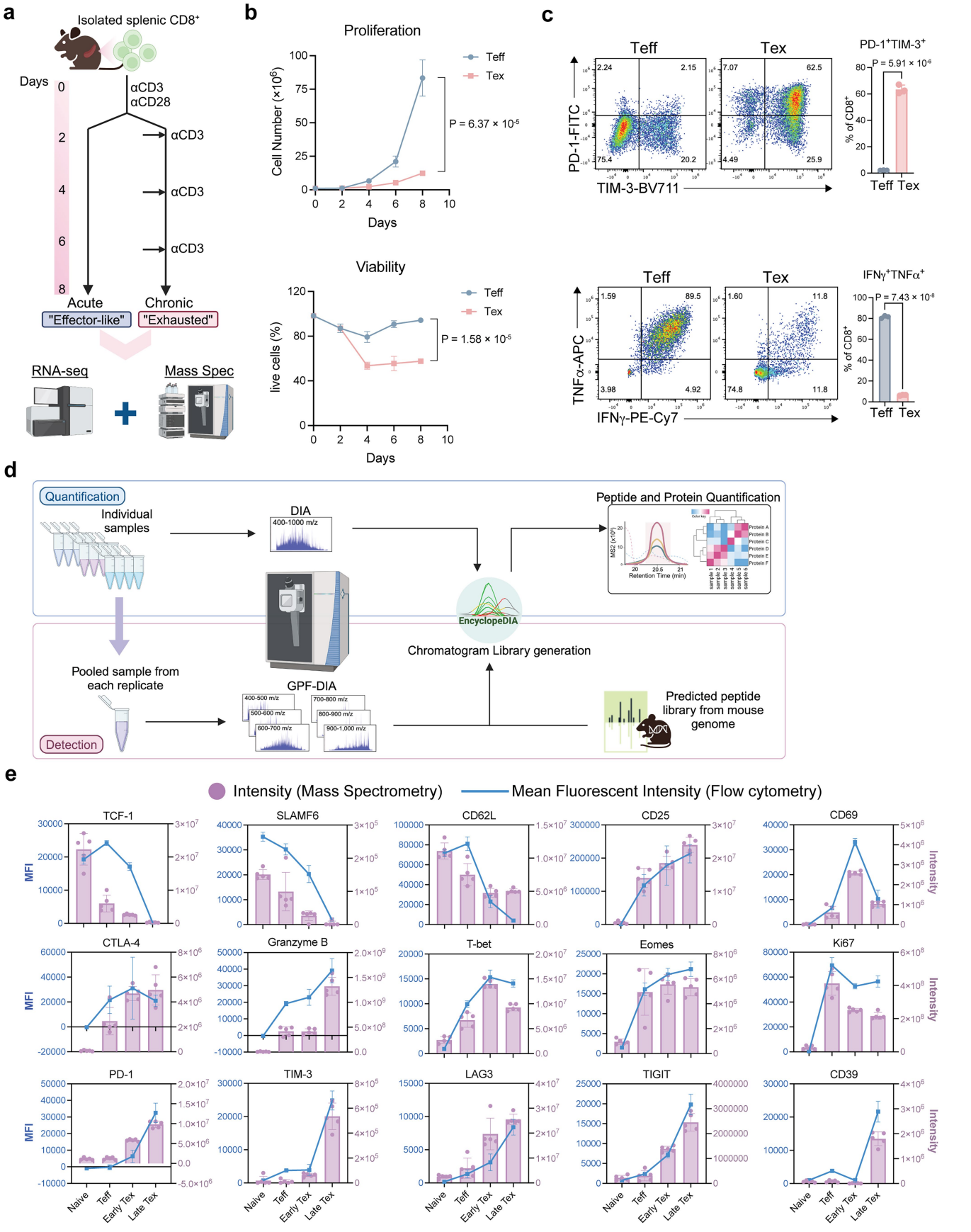

Extended Data Fig. 1 | See next page for caption.

Extended Data Fig. 1 | Study of the proteome changes during T cell exhaustion using an in vitro exhaustion model and quantitative mass spectrometry. **a**, Schematic diagram of generation of mouse $CD8^+$ Tex cells in vitro by repetitive TCR stimulations followed by parallel bulk RNA-seq and mass spectrometry. **b**, Proliferation and viability of Teff and Tex cells during the 8-day course post initial activation (*n = 4, two-way ANOVA*). **c**, Representative flow cytometry plots and statistics of the percentage of $PD\text{-}1^+TIM\text{-}3^+$ (upper) and $IFN\gamma^+TNF\alpha^+$ (bottom) cells over the total $CD8^+$ T cells in Teff versus Tex cells (*n = 3, two-tailed t test*). **d**, Schematic diagram of the workflow of the chromatogram library-based data-independent acquisition (DIA) mass spectrometry. **e**, Expression levels of indicated proteins measured by flow cytometry (line) and mass spectrometry (scatter-bar). Teff cells were day 3 acutely activated $CD8^+$ cells in vitro. Early and late Tex cells were day 3 and day 7 chronically activated $CD8^+$ T cells. *Data are presented as mean ± SD. Diagrams in **a** and **d** were created in BioRender. Wang, Y. (2025)* https://BioRender.com/n0ibmgq.

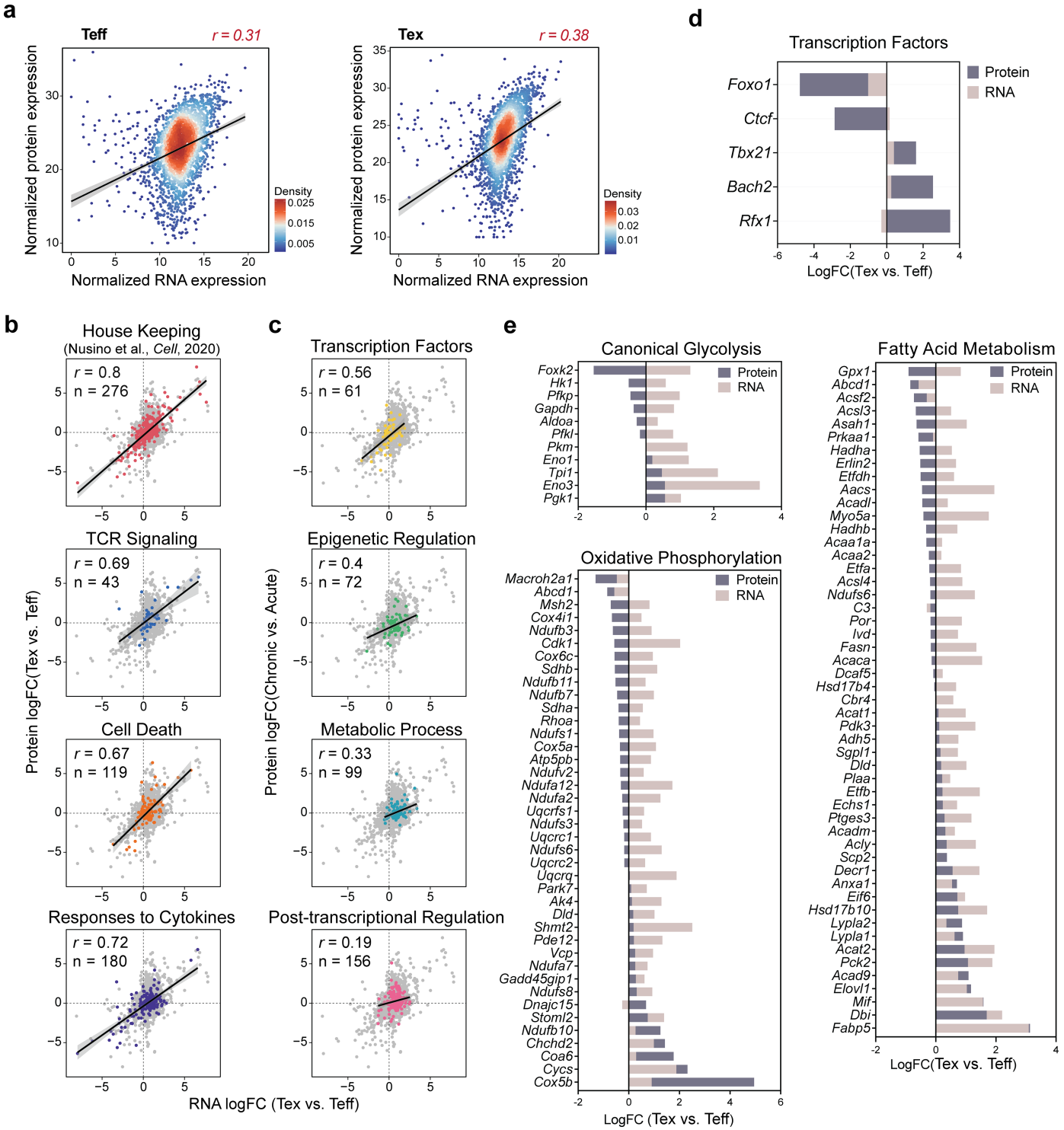

Extended Data Fig. 2 | Association as well as discordance between RNA and protein expression level in T cells. a, Correlation of RNA and protein expression levels of all detected molecules in Teff and Tex cells 8 days post initial activation. Each dot represents one molecule. A regression line with a shaded 95% confidence interval is shown. (*r: Pearson correlation coefficient*). **b-c**, Correlation between RNA levels and protein expression fold changes of molecules across one customer gene set and seven different gene ontologies between Tex and Teff cells (*r: Pearson correlation coefficient; n: numbers of proteins/genes mapped to each gene ontology, A regression line with a shaded 95% confidence interval is shown*). **d**, Bar plots of protein and mRNA expression changes of selected transcription factors in Tex vs Teff cells. **e**, Bar plots of protein and RNA expression changes of molecules belonging to the indicated gene ontologies in Tex vs. Teff cells.

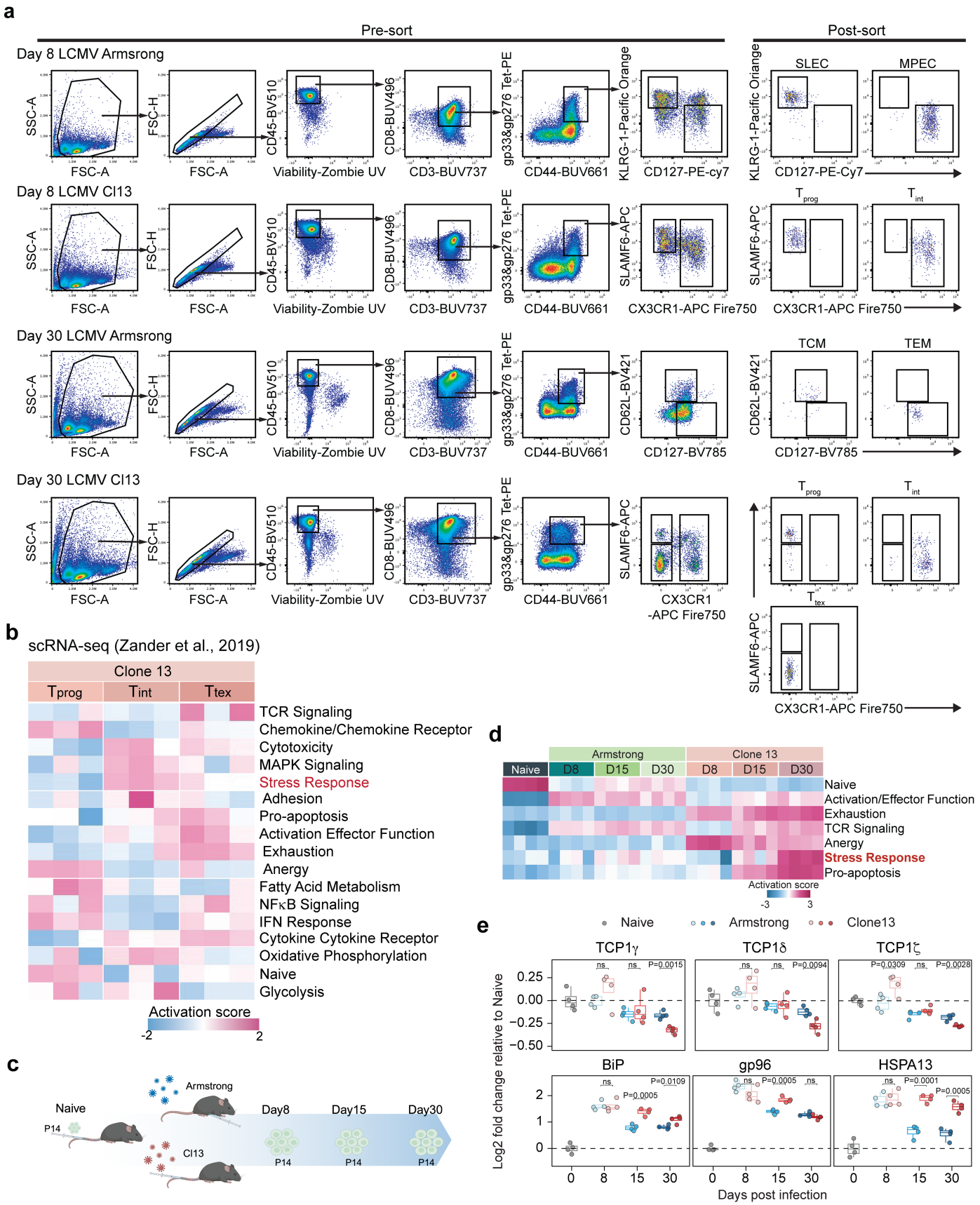

Extended Data Fig. 3 | See next page for caption.

Extended Data Fig. 3 | Study of T cell exhausion using an antigen-specific system against LCMV. a, Gating strategies for sorting antigen-specific $CD8^+$ T cells into different subpopulations from the spleens of LCMV infected mice. Tet, tetramer. **b**, Heatmap of expression levels of 17 gene signatures in $gp33^+$ T cell subpopulations on day 30 post LCMV Clone 13 infection (the scRNA-seq data were from Zander et al.). T_{prog}, T_{int}, T_{tex} subpopulations were determined based on their expression level of *Slamf6* and *Cx3cr1*. **c**, Schematic diagram of longitudinal proteome analysis of P14 T cells transferred to mice and harvested 8, 15 and 30 days after infection with LCMV Armstrong or Clone 13. *Created in BioRender. Wang, Y. (2025)* https://BioRender.com/n0ibmgq. **d**, Heatmap of expression levels of proteins belonging to different T cell signatures in P14 T cells from LCMV Armstrong or Clone 13 infected mice. **e**, Expression dynamics of protein chaperones in P14 cells analyzed as in **c** (*n = 4, two-tailed t test*). *Data are presented as box plots displaying the median (center line), 25th and 75th percentiles (bounds of the box), and minimum and maximum values (whiskers).*

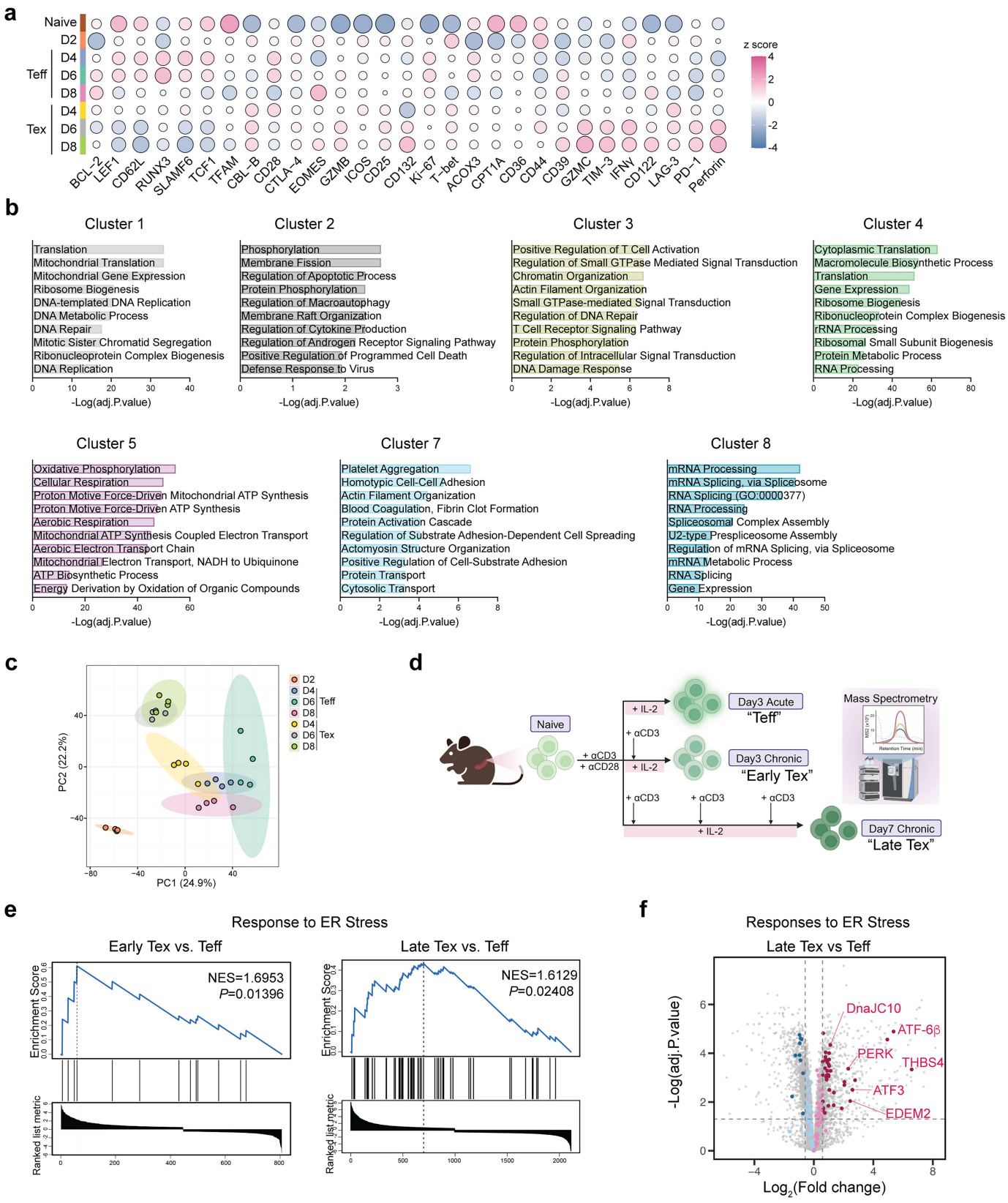

Extended Data Fig. 4 | See next page for caption.

Extended Data Fig. 4 | Mass spectrometry-based quantitative proteomics uncovers proteome changes during T cell exhaustion. a, Bubble plot of the expressions of proteins associated with T cell stemness, activation and exhaustion. Bubble color intensity is proportional to protein expression level. Bubble size is proportional to the absolute z-score value. **b**, Enrichment analysis of proteins in cluster 1–5 and 7, 8 by Enrichr (*one-sided Fisher's exact test with Benjamini–Hochberg correction*). Cluster 6 data was show in main Fig. 1. Top 10 significant gene ontologies are shown. **c**, PCA analysis of the proteome of *in vitro*-generated Teff and Tex cells at indicated time points. **d**, Schematic diagram of generating Teff, early and late Tex in vitro. *Created in BioRender. Wang, Y. (2025)* https://BioRender.com/n0ibmgq. **e**, Gene set enrichment analysis of differentially expressed proteins in early Tex versus Teff (top) and late Tex versus Teff cells (bottom). **f**, Volcano plots of differentially expressed proteins in late Tex versus Teff cells (*two-sided t-tests with Benjamini–Hochberg correction*). Proteins belonging to GO term "Responses to ER stress" are colored.

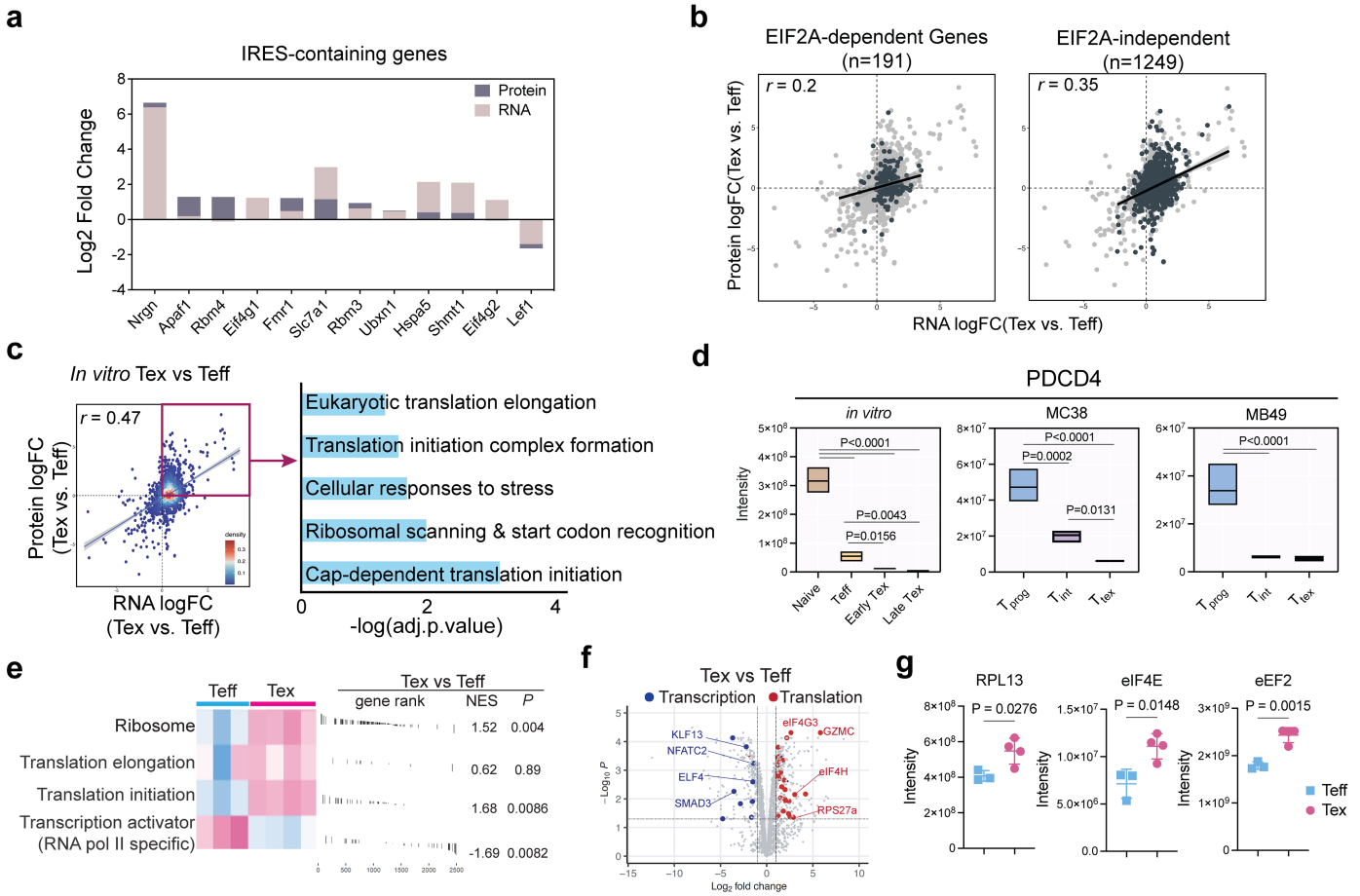

Extended Data Fig. 5 | Exhausted T cells do not have expected features of translational attenuation. a, Bar plot of protein and RNA expression changes of IRES motif-containing genes in Tex vs Teff cells 8 days post initial activation from the in vitro exhaustion model. **b**, Correlations of RNA and protein expression fold changes of EIF2A-dependent and EIF2A-independent genes in Tex vs Teff cells. A regression line with a shaded 95% confidence interval is shown. **c**, Enrichment analysis by Enrichr on proteins showing upregulation in both RNA and protein level (circled, left) in Tex versus Teff cells (*one-sided Fisher's exact test with Benjamini–Hochberg correction*). A regression line with a shaded 95% confidence interval is shown in the left panel. **d**, PDCD4 expression across different CD8$^+$ T cells subpopulations from in vitro exhaustion and in vivo tumor models by mass spectrometry (*n = 5 for* in vitro *model, n = 3 for MC38 and MB49 tumor models, one-way ANOVA*). Data are presented as mean (center line) and min to max (box bounds). **e**, The left panel is the heatmap of protein expression levels associated with selected Gene Ontology (GO) terms in *in vitro*-generated Teff and Tex cells 8 days post initial activation. Gene Set Enrichment Analysis (GSEA, right) compares Tex versus Teff cells, with normalized enrichment score (NES), gene rank distribution, and associated unadjusted P values are shown. P values were estimated using an adaptive multi-level split Monte Carlo scheme. **f**, Volcano plots of differentially expressed proteins in Tex versus Teff cells. Red: translation-related proteins; Blue: transcription-related proteins; Grey: other proteins (*two-sided t-tests with Benjamini–Hochberg correction*). **g**, Mass spectrometry analysis of protein expression levels of RPL13, eIF4E and eEF2 (*n = 3 for Teff and n = 4 for Tex, two-tailed t test*).

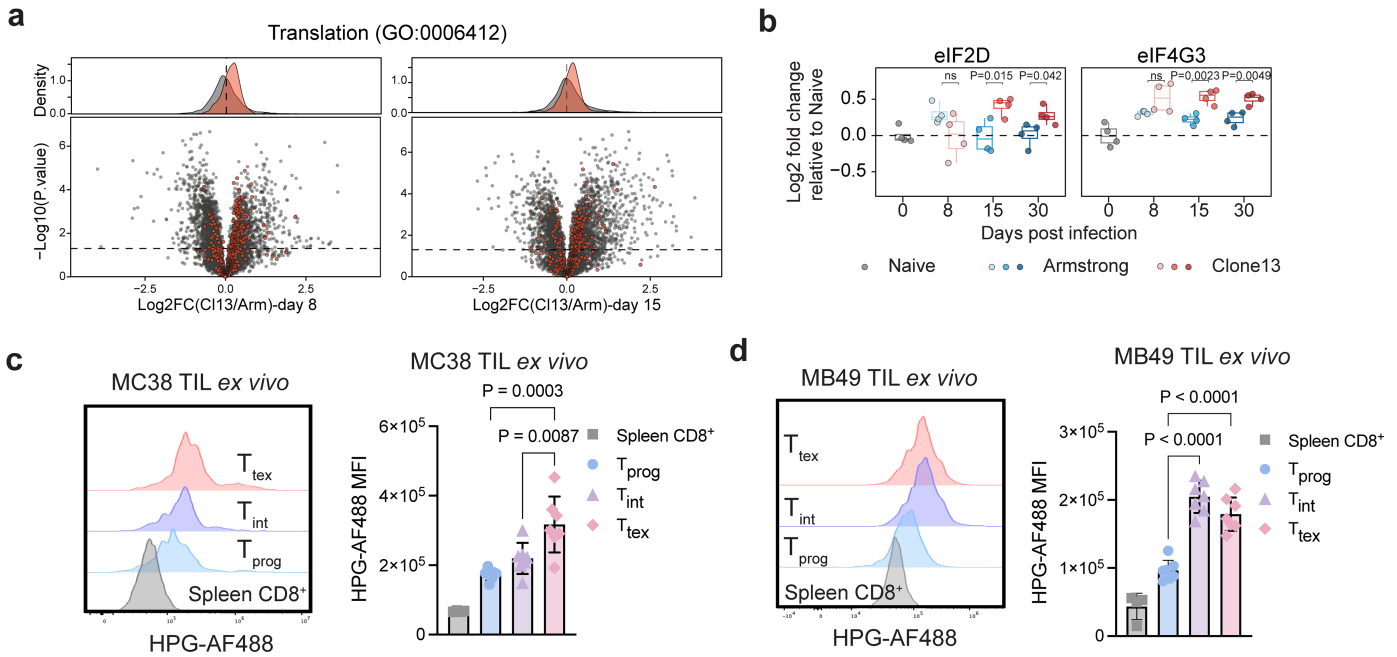

Extended Data Fig. 6 | Protein synthesis is upregulated in exhausted T cells in both tumor and chronic LCMV infection models. a, Volcano plots of differentially expressed proteins in P14 T cells from LCMV acute and chronic infections as described in Extended Data Fig. 3c. Proteins belonging to the protein translation (GO:0006412) are colored in red. **b**, eIF2D and eIF4G3 expression in P14 T cells from LCMV acute and chronic infections (*n = 4, multiple t test*). Data are presented as box plots displaying the median (center line), 25th and 75th percentiles (bounds of the box), and minimum and maximum values (whiskers). **c**-**d**, Flow cytometry histogram and bar plot of 30-min HPG incorporation ex vivo in tumor-infiltrating $CD8^+$ T cell subpopulations from mouse MC38 (**c**) and MB49 (**d**) tumors (spleen: *n = 4, TIL: n = 7, one-way ANOVA*). Data in **c** and **d** are presented as mean ± SD.

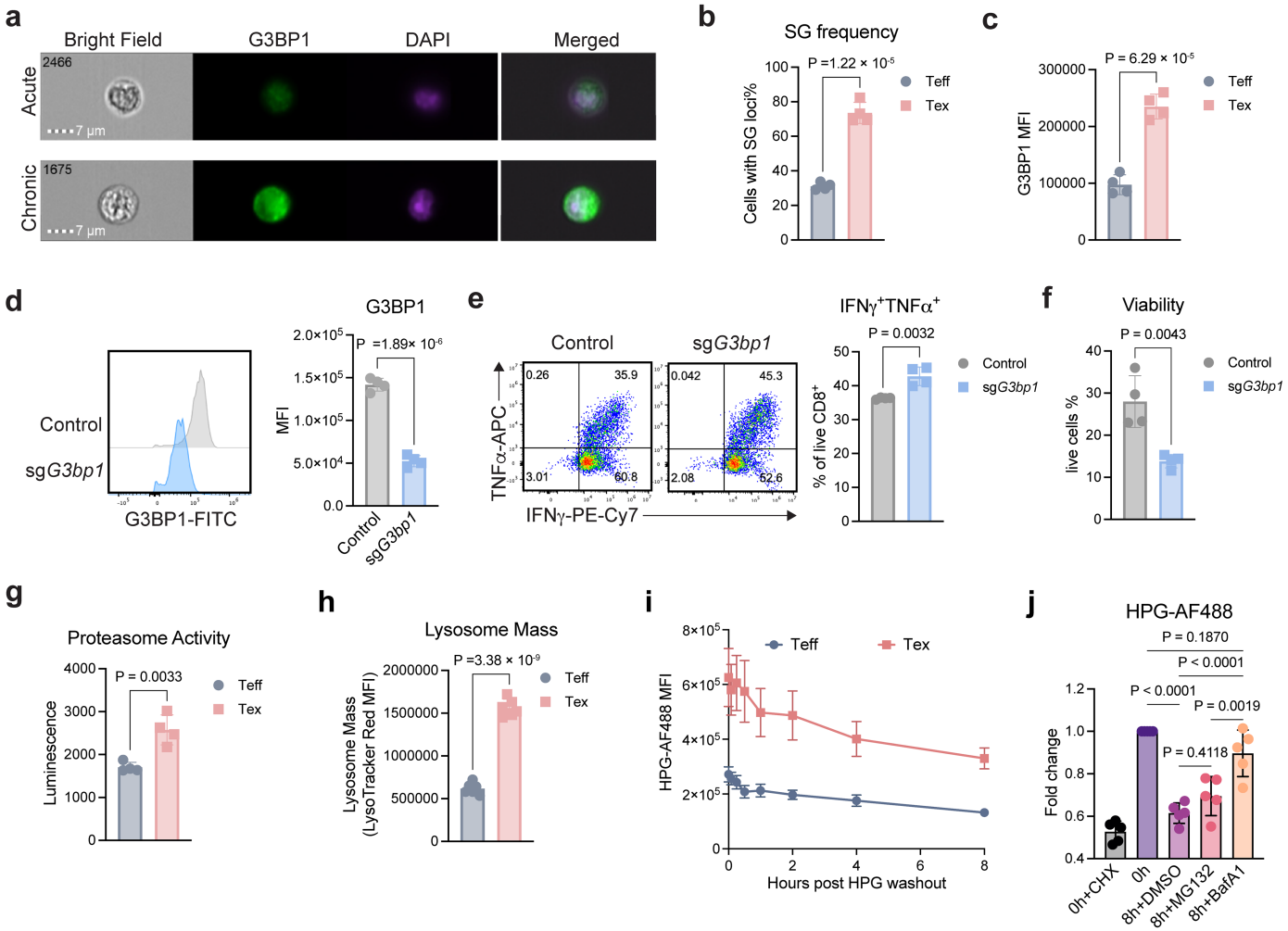

Extended Data Fig. 7 | Stress granules, proteasomal and lysosomal activities are increased in Tex cells. All experiments were performed using mouse Teff and Tex cells generated in vitro 8 days post initial activation. **a**, ImageStream analysis of G3BP1 stress granules (SGs) in Teff and Tex cells. **b**, Quantification of the frequency of G3BP1 SGs in Teff and Tex cells determined with Bright Detail Intensity by ImageStream analysis. At least 2,000 live cells were examined for each replicate ($n = 4$, *two-tailed t test*). **c**, Flow cytometry quantification of G3BP1 expression in Teff and Tex cells ($n = 4$, *two-tailed t test*). **d**, Representative flow cytometry plots and statistics of G3BP1 expression in *G3bp1* knockout and control wild-type Tex cells ($n = 4$, *two-tailed t test*). **e**, Representative flow cytometry plots and statistics of the percentage of IFNγ$^+$TNFα$^+$ cells out of the total CD8$^+$ T cells in *G3bp1* knockout and wild-type Tex cells ($n = 4$, *two-tailed t test*). **f**, Viability of *G3bp1* knockout and wild-type Tex cells ($n = 4$, *two-tailed t test*). **g**, Proteasomal activity in Teff and Tex cells ($n = 4$, *two-tailed t test*). **h**, Flow cytometry quantification of lysosome mass in Teff and Tex cells ($n = 6$, *two-tailed t test*). **i**, Degradation kinetics of newly synthesized proteins in Teff and Tex cells ($n = 3$). **j**, Fold changes of HPG MFI 8 h post "pulsing" with MG132, Bafilomycin A1(BafA1) or DMSO in Tex cells ($n = 5$, *one-way ANOVA*). Data in **b**-**h** and **j** are presented as mean ± SD. Data in **i** are presented as mean ± SEM.

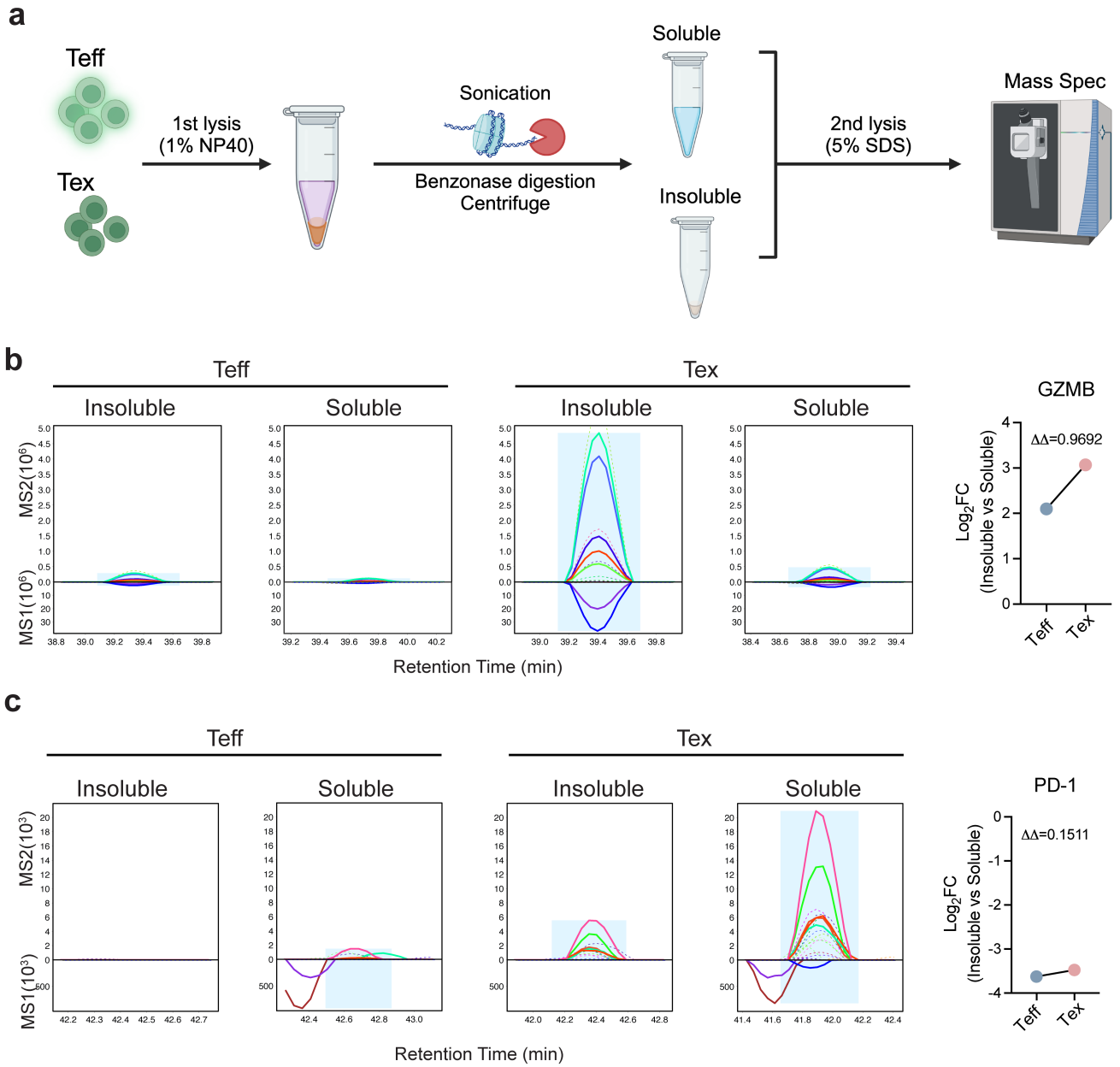

Extended Data Fig. 8 | Effector molecule granzyme B but not inhibitory receptor PD-1 is enriched in insoluble aggregates of Tex cells. a, Schematic diagram of fractionate soluble and insoluble proteins in the cell lysates of Teff and Tex cells 8 days post initial activation in vitro for mass spectrometry analysis. *Created in BioRender. Wang, Y. (2025)* https://BioRender.com/n0ibmgq. **b**, Representative chromatograms of the retention time and intensity for peptides indicative of granzyme B in insoluble and soluble protein. Raw intensity is on the y-axis and retention time in minutes is on the x-axis. Each colored line represents a fragment ion associated with the peptide for granzyme B. Solid lines indicate fragment ions used for quantitation. Dotted lines represent interfering ions that were excluded for quantitation. The plot on the far right showed the fold change of granzyme B in the insoluble over soluble fractions in Tex and Teff cells. ΔΔ: Tex[Log2FC(insoluble/soluble)] - Teff[Log2FC(insoluble/soluble)]. **c**, Representative chromatograms of the retention time and intensity for peptides indicative of PD-1 in the insoluble and soluble fractions. The fold changes of PD-1 in the insoluble over soluble fractions in Tex and Teff cells are also shown.

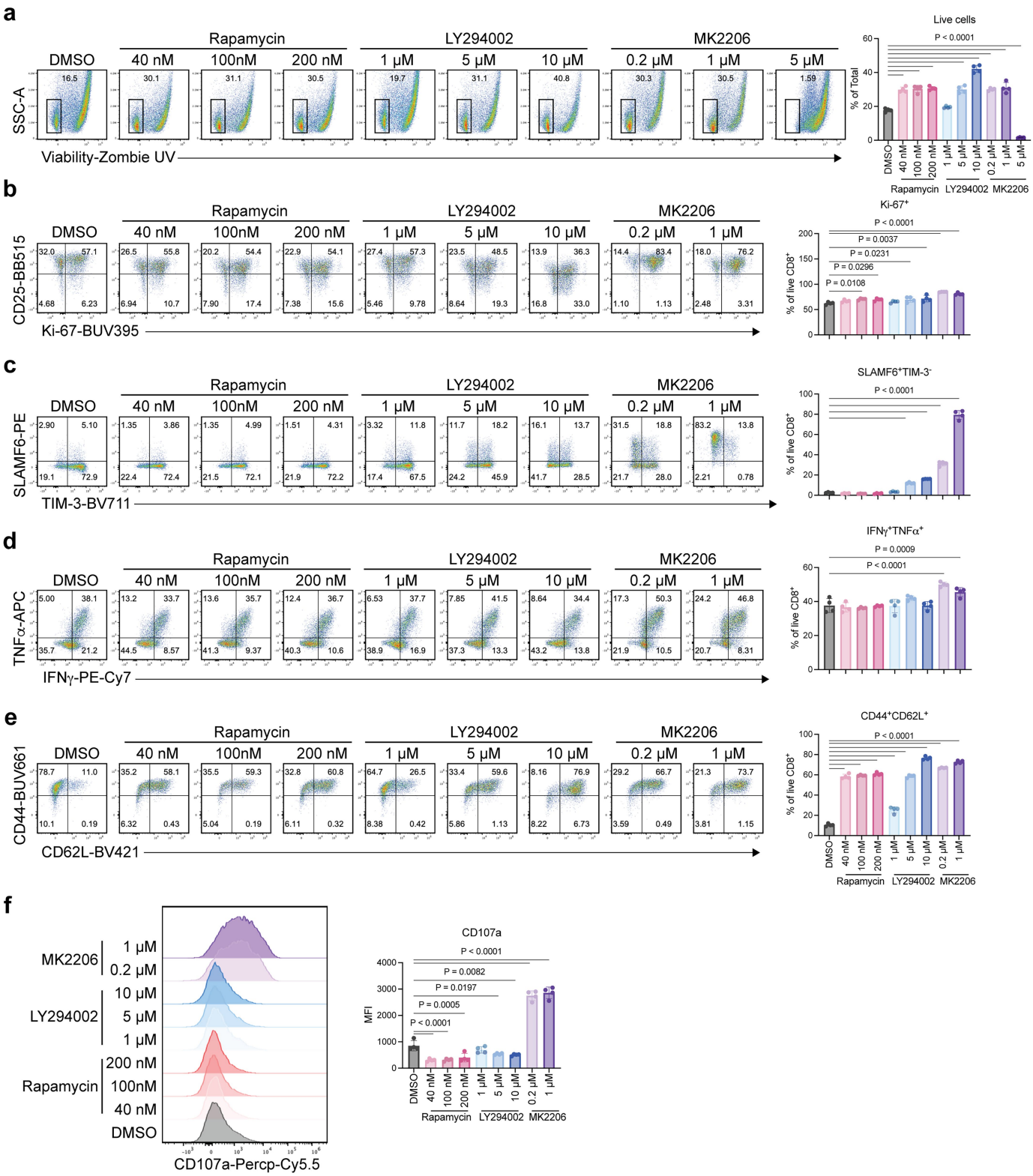

Extended Data Fig. 9 | Moderate attenuation of Akt signaling but not PI3K and mTOR pathways prevents T cell exhaustion without compromising cell survival and proliferation. Mouse CD8$^+$ T cells were first activated in vitro for 48 h, followed by chronic TCR stimulation in the presence of various pharmacological inhibitors and the final downstream analysis. **a-f**, Representative flow cytometry plots and statistics of the percentages of live cells (**a**), Ki67$^+$ population (**b**), SLAMF6$^+$TIM-3$^-$ population (**c**), IFNγ$^+$TNFα$^+$ population (**d**), CD44$^+$CD62L$^+$ population (**e**) and CD107a production (**f**). For measuring cytokine production (IFNγ, TNFα and CD107a), cells were rested for two additional days after 6-day treatment and restimulated with PMA/Ionomycin ($n = 4$, *one-way ANOVA*). *Data in* ***a*** *-* ***f*** *are presented as mean ± SD.*

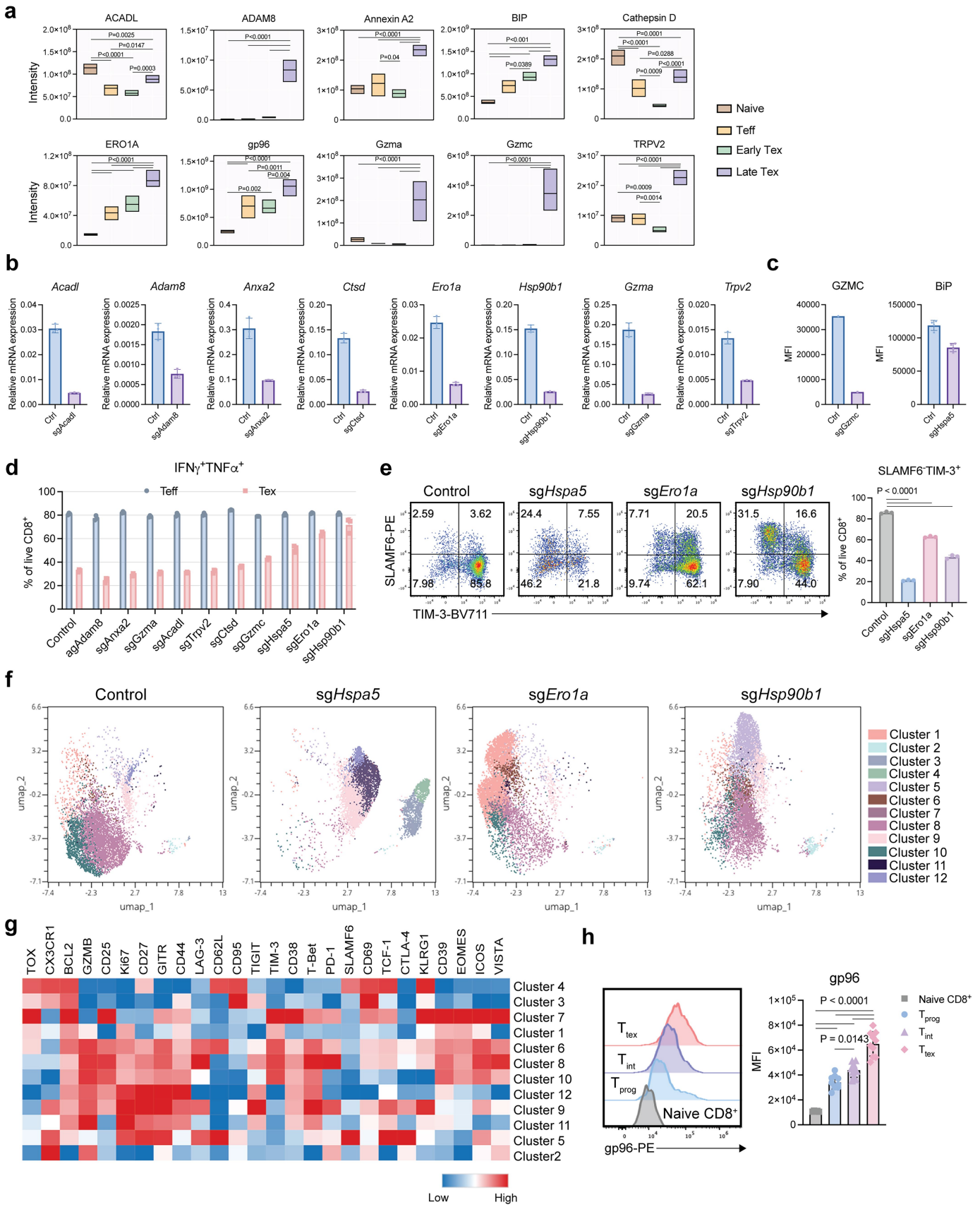

Extended Data Fig. 10 | See next page for caption.

Extended Data Fig. 10 | Impact of deletion of TexPSR chaperones on T cell exhaustion. Experiments were performed using in vitro exhausted T cells (**a**-**g**) and LCMV model in vivo (**h**). **a**, Expressions of the 10 candidate proteins in T cell exhaustion across 4 differentiation states as described in Extended Data Fig. 4d by mass spectrometry (*n = 5, one-way ANOVA*). Data are presented as mean (center line) and min to max (box bounds). **b**, Confirmation of CRISPR knockout of respective genes by RT-PCR. **c**, Confirmation of CRISPR knockout of indicated genes at the protein level by flow cytometry. **d**, Bar plot of the percentage of $IFN\gamma^+TNF\alpha^+$ cells out of the total $CD8^+$ T cells 8 days post CRISPR-Cas9 knockout of indicated genes and chronic stimulation (*n = 3, experiment was repeated three times*). **e**, Representative flow cytometry plot and percentages of $SLAMF6^-TIM\text{-}3^+$ population over total live $CD8^+$ T cells after *Hspa5*, *Ero1a* or *Hsp90b1* knockout or control (*n = 3, one-way ANOVA*). **f**, UMAP visualization of Tex cells with *Hspa5*, *Ero1a* or *Hsp90b1* knockout or control T cells analyzed with 26 markers associated with T cell activation and exhaustion indicated in **g** by multi-spectral flow cytometry. **g**, Heatmap of expression pattern of 26 markers across 12 cell clusters. Data was shown using all concatenated cells. **h**, gp96 expression in different Tex subsets gated on $CD44^+PD\text{-}1^+$ $CD8^+$ T cells from day 30 LCMV Clone 13 infected wild type mouse spleens. Naïve $CD8^+$ T cells were $CD44^-CD8^+$ T cells from uninfected mice (*n = 5 for naïve* $CD8^+$, *n = 10 for* T_{prog}, T_{int} *and* T_{tex}, *one-way ANOVA*). *Data in* ***b***-***e*** *and* ***h*** *are presented as mean ± SD.*

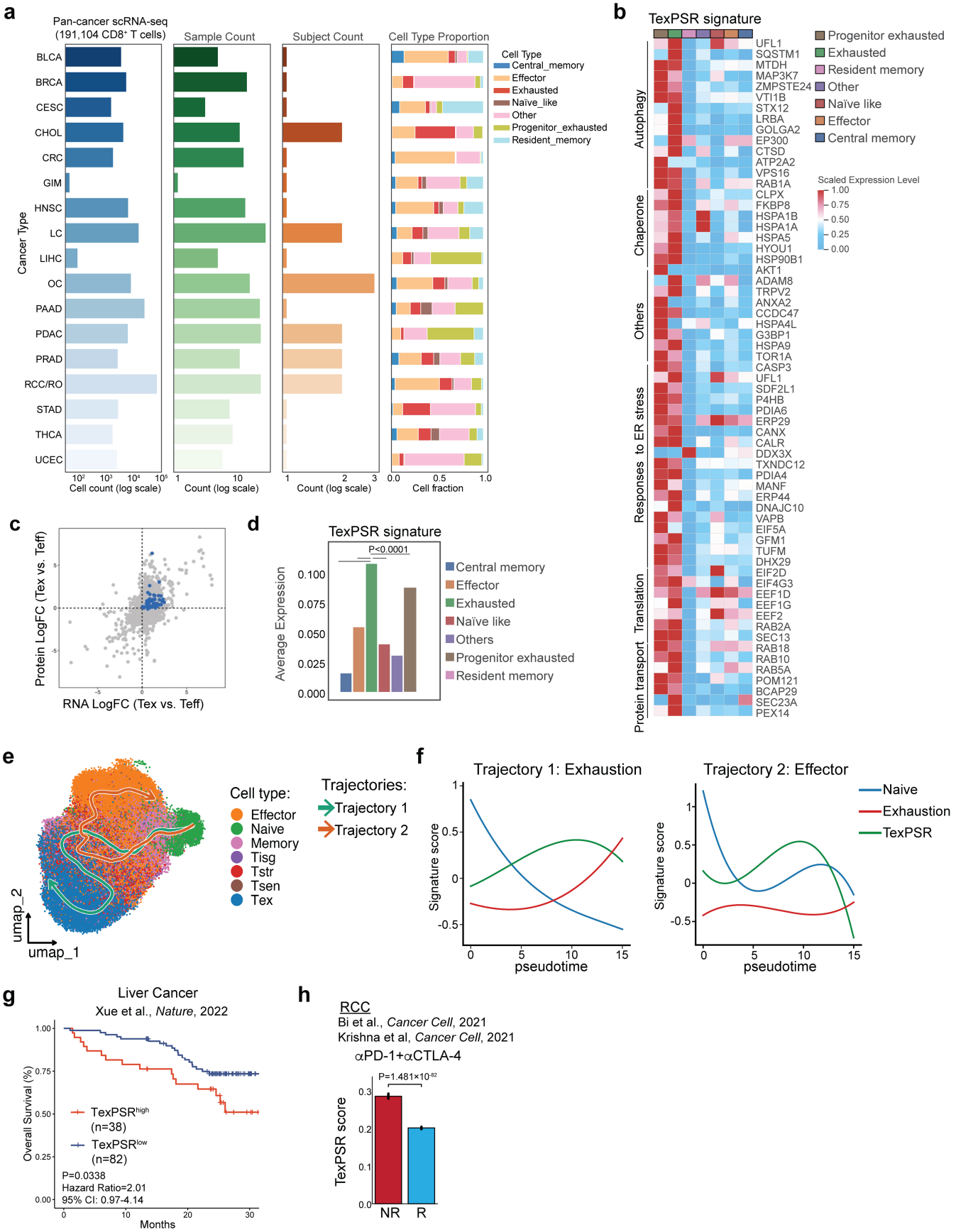

Extended Data Fig. 11 | See next page for caption.

Extended Data Fig. 11 | Patients with high TexPSR signature in tumor-infiltrating T cells do poorly in response to immunotherapy. a, Overview of $CD8^+$ T cell counts and subtype distributions across different cancer types from integrated analysis of publicly available pan-cancer scRNA-seq datasets. Left panel: total number of $CD8^+$ T cells detected in each cancer type, plotted on a logarithmic scale. Middle left panel: sample counts in each cancer type, plotted on a logarithmic scale. Middle right panel: number of independent studies for each cancer type. Right panel: $CD8^+$ T cell subtype proportion. BLCA: bladder urothelial carcinoma; BRCA: breast invasive carcinoma; CESC: cervical squamous cell carcinoma and endocervical adenocarcinoma; CHOL: cholangiocarcinoma; CRC: colorectal cancer; GIM: gastric and intestinal malignancies; HNSC: head and neck squamous cell carcinoma; LC: lung cancer; LIHC: liver hepatocellular carcinoma; OC: ovarian cancer; PAAD: pancreatic adenocarcinoma; PDAC: pancreatic ductal adenocarcinoma; PRAD: prostate adenocarcinoma; RCC/CRCC: renal cell carcinoma/clear cell renal cell carcinoma; STAD: stomach adenocarcinoma; THCA: thyroid carcinoma; UCEC: uterine corpus endometrial carcinoma. **b**, Heatmap showing the expression level of TexPSR signature genes across various T cell populations. **c**, Correlation of RNA and protein expression fold changes of TexPSR signature genes between Tex versus Teff cells from the in vitro exhaustion model. **d**, TexPSR signature scores across different T cell subpopulations (*two-sided Wilcoxon rank sum test*). **e**, UMAP embedding of scRNA-seq data from T cells colored by annotated cell types. Overlaid are RNA velocity-based trajectories, inferred with the Slingshot algorithm, delineating two major differentiation pathways: Trajectory 1 (teal) toward exhaustion and Trajectory 2 (orange) toward effector differentiation. **f**. Signature scores along pseudotime for each trajectory. Trajectory 1 (left) shows decreasing Naive and increasing Exhaustion and TexPSR scores, consistent with an exhaustion trajectory. Trajectory 2 (right) shows dynamic changes in TexPSR and Naive scores, indicative of an alternative effector trajectory. **g**, Kaplan-Meier survival curves for patients with liver cancer stratified by high vs. low TexPSR signature, calculated from the $CD8^+$ T cell scRNAseq data. P values were calculated using a univariate Cox proportional hazards model. **h**, TexPSR scores in scRNA-seq datasets of $CD8^+$ T cells from non-responders (NR) and responders (R) in response to αPD-1 combined with αCTLA-4 therapy for RCC (*NR: n = 5354 cells from 6 patients, R: n = 15207 cells from 9 patients*). *Data are presented as mean ± SEM, and statistical significance was determined using two-sided Wilcoxon rank sum tests*.

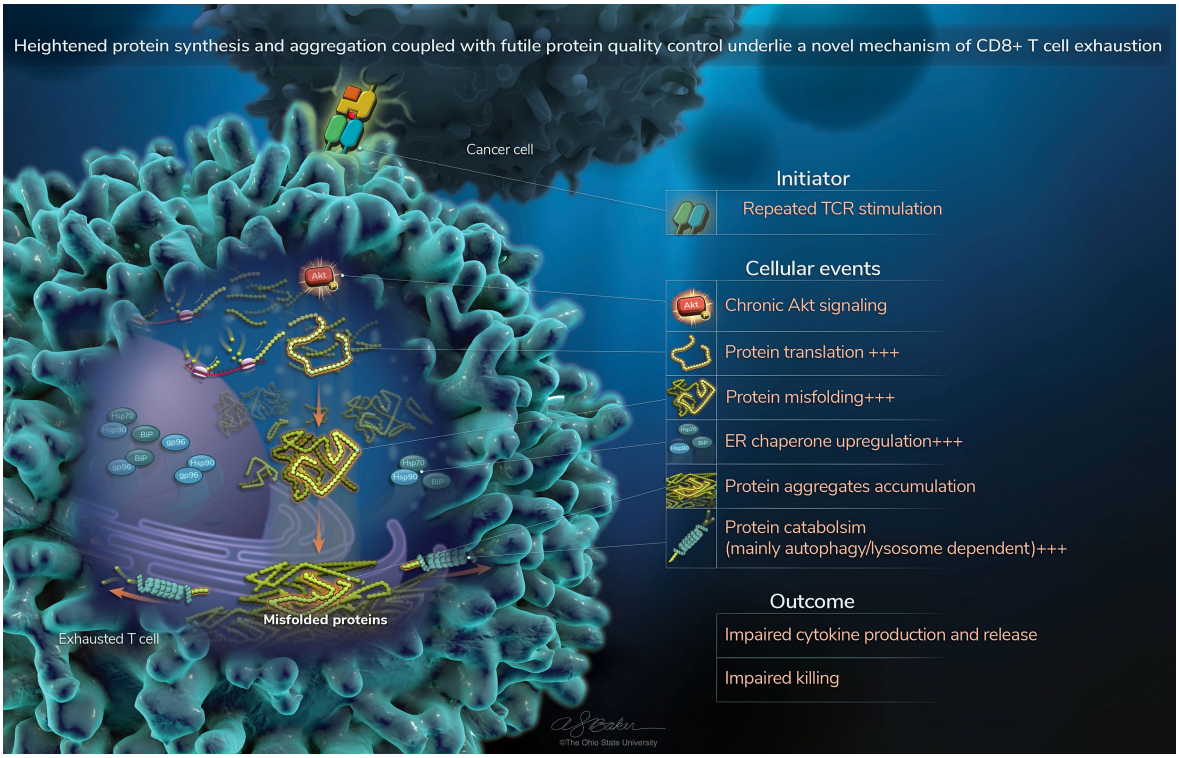

Extended Data Fig. 12 | Working model of TexPSR as a mechanistic driver of CD8⁺ T cell exhaustion. The model presented illustrates a cancer cell at the top interacting with an exhausted T cell at the bottom through the MHC class I–T cell receptor complex. The intracellular events inside of the Tex cells underscore key novel findings from the study, which collectively elucidate a proteotoxic stress response (PSR) driving T cell exhaustion, a phenomenon we term TexPSR. TexPSR is characterized by an elevated rate of protein synthesis, the accumulation of intracellular protein aggregates, the upregulation of specific endoplasmic reticulum (ER) chaperones, and an accelerated protein catabolism pathway. Central to these processes is the sustained activation of AKT signaling, which orchestrates this complex proteotoxic environment. These findings not only provide deeper insight into the molecular mechanisms of T cell dysfunction within the tumor microenvironment but also open avenues for possible therapeutic strategies aimed at mitigating TexPSR to restore immune cell function in cancer immunotherapy. The figure was reproduced with the permission of The Ohio State University.

nature portfolio

Corresponding author(s): Zihai Li

Last updated by author(s): Jul 24, 2025

Reporting Summary

Nature Portfolio wishes to improve the reproducibility of the work that we publish. This form provides structure for consistency and transparency in reporting. For further information on Nature Portfolio policies, see our Editorial Policies and the Editorial Policy Checklist.

Statistics

For all statistical analyses, confirm that the following items are present in the figure legend, table legend, main text, or Methods section.

n/a	Confirmed	
☐	☒	The exact sample size (*n*) for each experimental group/condition, given as a discrete number and unit of measurement
☐	☒	A statement on whether measurements were taken from distinct samples or whether the same sample was measured repeatedly
☐	☒	The statistical test(s) used AND whether they are one- or two-sided *Only common tests should be described solely by name; describe more complex techniques in the Methods section.*
☐	☒	A description of all covariates tested
☐	☒	A description of any assumptions or corrections, such as tests of normality and adjustment for multiple comparisons
☐	☒	A full description of the statistical parameters including central tendency (e.g. means) or other basic estimates (e.g. regression coefficient) AND variation (e.g. standard deviation) or associated estimates of uncertainty (e.g. confidence intervals)
☐	☒	For null hypothesis testing, the test statistic (e.g. *F*, *t*, *r*) with confidence intervals, effect sizes, degrees of freedom and *P* value noted *Give P values as exact values whenever suitable.*
☒	☐	For Bayesian analysis, information on the choice of priors and Markov chain Monte Carlo settings
☒	☐	For hierarchical and complex designs, identification of the appropriate level for tests and full reporting of outcomes
☐	☒	Estimates of effect sizes (e.g. Cohen's *d*, Pearson's *r*), indicating how they were calculated

Our web collection on statistics for biologists contains articles on many of the points above.

Software and code

Policy information about availability of computer code

Data collection	Flow cytometry experiments were performed using Cytek Aurora flow cytometer or ImageStream imaging flow cytometer. Cell sorting experiments were performed using Cytek Cell Sorter. Confocal microscopy images were collected by Olympus FV3000 microscope. Proteomics data were collected using an Easy-nLC 1200 coupled to an Thermo Exploris 480 tandem mass spectrometer (Thermo Fisher) or an UltiMate 3000 UHPLC coupled to a Thermo Fusion tandem mass spectrometer (Thermo Fisher). Bulk RNAseq was performed using Illumina NovaSeq platform with a depth of 50 million reads per sample.
Data analysis	Flow cytometry analysis were performed using FlowJo (version 10.10) or OMIQ (www.omiq.ai). Imaging flow cytometry data generated by ImageStream were analyzed using IDEAS (v6.2) software. Numerical data were exported and analyzed using GraphPad Prism v10. Confocal microscopy images were analyzed by OlyVIA (v4.2) software. Raw files of proteomics data were converted using MSConvert in the Proteowizard package (version 3.0.20169) and then searched using EncyclopeDIA (version 2.12.31). Bulk RNA-seq sequences were checked, trimmed, and filtered by using Fastp (v0.23.4). The filtered reads were mapped to the mouse reference genome mm10 using HISAT2 (v2.2.1), and samtools (v1.17) was used to convert and sort BAM files. Lastly, the subread tool (v2.0.6) was used for gene quantification and generating the raw expression matrix. Raw expression data was first log normalized, and the Limma R package (v3.56.2) was used to fit the model and perform differential expression analysis. Scanpy package (v1.9.5) and scVI Python package (scvi-tools v1.0.4) were used for single-cell RNAseq data analysis. RNA Velocities were computed using the scVelo toolkit (v0.3.3). Tidyverse (v1.3.1), EnrichR(https://maayanlab.cloud/Enrichr), heatmaply R package (v1.4.2), Morpheus (https://software.broadinstitute.org/morpheus) were used for plotting figures.

For manuscripts utilizing custom algorithms or software that are central to the research but not yet described in published literature, software must be made available to editors and reviewers. We strongly encourage code deposition in a community repository (e.g. GitHub). See the Nature Portfolio guidelines for submitting code & software for further information.

Data

Policy information about availability of data

All manuscripts must include a data availability statement. This statement should provide the following information, where applicable:

- Accession codes, unique identifiers, or web links for publicly available datasets
- A description of any restrictions on data availability
- For clinical datasets or third party data, please ensure that the statement adheres to our policy

Proteomics data is available at the MassIVE repository (MSV000098609) and through ProteomeXchange (PXD066433). Normalized protein expression data is provided in Supplementary Table S3. Bulk RNA sequencing data from this paper is deposited to NCBI GEO database with identifier GSE303401. Scripts generated for analysis are available at https://doi.org/10.5281/zenodo.16323779.

Research involving human participants, their data, or biological material

Policy information about studies with human participants or human data. See also policy information about sex, gender (identity/presentation), and sexual orientation and race, ethnicity and racism.

Reporting on sex and gender	*Use the terms sex (biological attribute) and gender (shaped by social and cultural circumstances) carefully in order to avoid confusing both terms. Indicate if findings apply to only one sex or gender; describe whether sex and gender were considered in study design; whether sex and/or gender was determined based on self-reporting or assigned and methods used.* *Provide in the source data disaggregated sex and gender data, where this information has been collected, and if consent has been obtained for sharing of individual-level data; provide overall numbers in this Reporting Summary. Please state if this information has not been collected.* *Report sex- and gender-based analyses where performed, justify reasons for lack of sex- and gender-based analysis.*
Reporting on race, ethnicity, or other socially relevant groupings	*Please specify the socially constructed or socially relevant categorization variable(s) used in your manuscript and explain why they were used. Please note that such variables should not be used as proxies for other socially constructed/relevant variables (for example, race or ethnicity should not be used as a proxy for socioeconomic status).* *Provide clear definitions of the relevant terms used, how they were provided (by the participants/respondents, the researchers, or third parties), and the method(s) used to classify people into the different categories (e.g. self-report, census or administrative data, social media data, etc.)* *Please provide details about how you controlled for confounding variables in your analyses.*
Population characteristics	*Describe the covariate-relevant population characteristics of the human research participants (e.g. age, genotypic information, past and current diagnosis and treatment categories). If you filled out the behavioural & social sciences study design questions and have nothing to add here, write "See above."*
Recruitment	*Describe how participants were recruited. Outline any potential self-selection bias or other biases that may be present and how these are likely to impact results.*
Ethics oversight	*Identify the organization(s) that approved the study protocol.*

Note that full information on the approval of the study protocol must also be provided in the manuscript.

Field-specific reporting

Please select the one below that is the best fit for your research. If you are not sure, read the appropriate sections before making your selection.

☒ Life sciences ☐ Behavioural & social sciences ☐ Ecological, evolutionary & environmental sciences

For a reference copy of the document with all sections, see nature.com/documents/nr-reporting-summary-flat.pdf

Life sciences study design

All studies must disclose on these points even when the disclosure is negative.

Sample size	No statistical methods were used to predetermine sample size. Sample sizes were determined based on pilot experiments and previously published results with similar experimental models (Kwon et al., Science Immunology, 2022; Song et al., Cancer Discovery, 2025). The exact n numbers for biological replicates used in the study are indicated in the respective figure legends.
Data exclusions	Proteomic replicates with technical issues related to sample preparation, data acquisition, or instrument performance were excluded. No data were excluded from other experiments.
Replication	All experiments were independently performed at least twice and demonstrated the same phenotypes to ensure reproducibility.
Randomization	Age-matched mice were randomly assigned to experimental groups in tumor experiments and LCMV infection experiments. For genetically modified mice (e.g., E8iCre-gp96 flox/flox), group allocation was based on genotype and therefore not randomized. Randomization was not applicable to other experiments where different treatments were applied to materials derived from the same sample for each replicate for

paired comparisons.

Blinding

Imaging flow cytometry, proteomics and RNAseq data collection and analysis was performed blindly. Mouse tumor and viral infection experiments were performed blindly to treatment groups or genotypes. Blinding was not conducted for other experiments because the same person performed the experiments and analyzed results.

Reporting for specific materials, systems and methods

We require information from authors about some types of materials, experimental systems and methods used in many studies. Here, indicate whether each material, system or method listed is relevant to your study. If you are not sure if a list item applies to your research, read the appropriate section before selecting a response.

Materials & experimental systems

n/a	Involved in the study
☐	☒ Antibodies
☐	☒ Eukaryotic cell lines
☒	☐ Palaeontology and archaeology
☐	☒ Animals and other organisms
☒	☐ Clinical data
☒	☐ Dual use research of concern
☒	☐ Plants

Methods

n/a	Involved in the study
☒	☐ ChIP-seq
☐	☒ Flow cytometry
☒	☐ MRI-based neuroimaging

Antibodies

Antibodies used

A detailed list of antibodies used in this study is provided in Supplementary Table S1 with fluorochrome, clone, dilution and source the antibodies.

Validation

All antibodies used in this study were purchased or obtained from well-recognized vendors and the validation from source vendor is provided in Supplementary Table S1.

Eukaryotic cell lines

Policy information about cell lines and Sex and Gender in Research

Cell line source(s)

MC38 cell line was purchased from Kerafast (#ENH204-FP). MB49 cell line was purchased from Sigma-Aldrich (#SCC148). MB49-gp33 cell line was kindly shared by Dr. Weiguo Cui at Northwestern University. B16-OVA cell line was generated as described previously (Budhu et al., Sci Signal, 2017). HEK293T cell line was purchased from ATCC (#CRL-3216).

Authentication

No further authentications were conducted in the laboratory.

Mycoplasma contamination

All cell lines were tested negative for mycoplasma contamination.

Commonly misidentified lines
(See ICLAC register)

No commonly misidentified cell lines were used in the study.

Animals and other research organisms

Policy information about studies involving animals; ARRIVE guidelines recommended for reporting animal research, and Sex and Gender in Research

Laboratory animals

Wildtype C57BL/6J mice (strain #000664) purchased from Jackson Laboratory. CD8-specific gp96 deficient mice were generated by crossing E8i-Cre purchased from Jackson Laboratory (strain #008766) and Hsp90b1flox/flox mice previously generated and described by our group (Yang et al., Immunity, 2007). P14 mouse was a gift from Dr. Weiguo Cui at Northwestern University. OT-1 (strain #003831) and Rag2-/- (strain #033526) mice were purchased from Jackson Laboratory. 6-8-week-old mice were used for experiments. All mice used in this study were housed at the Ohio state University animal facility. Ambient temperature was kept in a range of 68-76 °F, relative humidity 30-70% and a 12-hour light/dark cycle (lights on from 6am to 6pm).

Wild animals

No wild animals were used in this study.

Reporting on sex

The results in this study are not restricted to one sex because both male and female mice were used and demonstrated similar phenotypes.

Field-collected samples

No samples were collected from the field.

Ethics oversight

All procedures were performed in strict accordance with the recommendations in the Guide for the Care and Use of Laboratory

Ethics oversight	Animals of the National Institutes of Health. The protocol was approved by the Committee on the Ethics of Animal Experiments of the Ohio State University.

Note that full information on the approval of the study protocol must also be provided in the manuscript.

Plants

Seed stocks	*Report on the source of all seed stocks or other plant material used. If applicable, state the seed stock centre and catalogue number. If plant specimens were collected from the field, describe the collection location, date and sampling procedures.*
Novel plant genotypes	*Describe the methods by which all novel plant genotypes were produced. This includes those generated by transgenic approaches, gene editing, chemical/radiation-based mutagenesis and hybridization. For transgenic lines, describe the transformation method, the number of independent lines analyzed and the generation upon which experiments were performed. For gene-edited lines, describe the editor used, the endogenous sequence targeted for editing, the targeting guide RNA sequence (if applicable) and how the editor was applied.*
Authentication	*Describe any authentication procedures for each seed stock used or novel genotype generated. Describe any experiments used to assess the effect of a mutation and, where applicable, how potential secondary effects (e.g. second site T-DNA insertions, mosiacism, off-target gene editing) were examined.*

Flow Cytometry

Plots

Confirm that:

☒ The axis labels state the marker and fluorochrome used (e.g. CD4-FITC).

☒ The axis scales are clearly visible. Include numbers along axes only for bottom left plot of group (a 'group' is an analysis of identical markers).

☒ All plots are contour plots with outliers or pseudocolor plots.

☒ A numerical value for number of cells or percentage (with statistics) is provided.

Methodology

Sample preparation	To prepare single cell suspensions of mouse tumor samples, isolated tumors were chopped and washed with PBS before incubation with Collagenase I (200 U/ml, Worthington #LS004196) in serum-free RPMI-1640 for 30 min at 37 °C with gentle agitation. After digestion, 2% BSA in PBS were added to cell suspensions to neutralize collagenase. Cell suspensions were washed with PBS and filtered through a 70-µm nylon filter. Single cell suspensions were centrifuged and resuspended in PBS for downstream assays. For cell sorting, immune cells were enriched using mouse TIL CD45 positive selection kit (STEMCELL #100-0350) Dead cells were stained by Live/Dead fixable blue (Invitrogen #L23105) or Zombie UV (BioLegend #423108) at 4 °C for 15 min. Cells were washed with FACS buffer twice and surface molecule staining antibody cocktail was applied for 30 minutes in 4 °C. After incubation, cells were washed twice with FACS buffer and then fixed and permeabilized using Foxp3 fixation and permeabilization kit (eBioscience #00-5523-00) overnight. After overnight fixation, cells were washed twice in the permeabilization buffer, and the intracellular staining antibody cocktail was added to the cells. After 2 hours of room temperature staining, cells were washed twice with FACS buffer and analyzed. For protein aggregation staining, cells were washed with HBSS (Sigma-Aldrich #H6648) twice and stained with 100 nM NIAD-4 (Cayman #18520) or 50 µM CRANAD-2 (Cayman #19814) in HBSS for 30 min at 37 °C and 5% CO2. Cells were next stained by Live/Dead fixable Near IR (Invitrogen #L34975) at 4 °C for 15 min, followed by fixation with 4% formaldehyde (BD Biosciences) for 15 min and DAPI staining for 5 min at room temperature. For stress granule analysis, cells were harvested and stained by Live/Dead fixable NIR, followed by fixation in BD CytofixTM fixation buffer (BD Biosciences #554655) for 15 min and permeabilization using Foxp3 fix/perm kit for 30 min at room temperature. Cells were then stained with anti-G3BP1 antibody (Proteintech #13057-2-AP) in perm buffer for 1 h at room temperature and then FITC-conjugated anti-Rabbit antibody for 30 min. DAPI was added to the cell suspension and incubated for 5 min. Gating strategy for sorting antigen specific CD8+ T cells in LCMV models is described in Extended Data Fig. 3a. For in vitro assays, cells were first identified by FSC-A/SSC-A scatters and then singlets based on FSC-A/FSC-H and SSC-A/SSC-H. Live cells were gated based on the absence of vialibity dye staining and analyzed.
Instrument	Cytek Aurora, Cytek Cell Sorter, ImageStream
Software	FlowJo (v10.10), OMIQ (www.omiq.ai), IDEAS (v6.2)
Cell population abundance	For sorting subpopulation of CD8+ T cells from spleens of LCMV models or tumors of MC38 or MB49 models, cells were sorted using "purity" mode. Purity of post-sorted cells were checked by flow cytometry and was over 96%.
Gating strategy	Gating strategy for sorting antigen specific CD8+ T cells in LCMV models is described in Extended Data Fig. 3a. For experiments using in vitro stimulated mouse CD8+ primary T cells, cells were first identified by FSC-A/SSC-A scatters and then singlets based on FSC-A/FSC-H and SSC-A/SSC-H. Live cells were gated based on the absence of viability dye staining and

analyzed. For analyzing CD8+ T cells from mouse tumors or spleens, CD8+ T cells were first gated using FSC-A/SSC-A and then FSC-A/FSC-H to exclude doublets. Live CD45+ were gated as total immune cells followed by identifying CD8+ T cells as CD3+ CD8+ CD4-. Antigen-specific CD8+ T cells were gated based on CD44hi cells.

☒ Tick this box to confirm that a figure exemplifying the gating strategy is provided in the Supplementary Information.